Elevated synaptic PKA activity and abnormal striatal dopamine signaling in *Akap11* mutant mice, a genetic model of schizophrenia and bipolar disorder

Bryan J. Song[1,11,*], Yang Ge[1,11], Ally Nicolella[1], Min Jee Kwon[1], Bart Lodder[2,3], Kevin Bonanno[4], Antia Valle-Tojeiro[4], Kira Perzel Mandell[1], John Adeleye[1], Chuhan Geng[1], Sahana Natarajan[1], Inès Picard[1], Nate Shepard[1], Sameer Aryal[1], Zohreh Farsi[1], Xiao-Man Liu[1], Nader Morshed[1,5], Naeem M Nadaf[1], Horia Pribiag[1], Sean K Simmons[1], D.R. Mani[4], Beth Stevens[1,5,6], Evan Z. Macosko[1,7], Joshua Z. Levin[1], Bernardo L. Sabatini[3,8], Hasmik Keshishian[4], Steven A. Carr[4], Borislav Dejanovic[1,9], Adam J. Granger[1,*] & Morgan Sheng[1,10,*]

1 The Stanley Center for Psychiatric Research, The Broad Institute of MIT and Harvard, Cambridge, MA, USA
2 Brain Center, Department of Translational Neuroscience, University Medical Center Utrecht and University Utrecht, the Netherlands
3 Department of Neurobiology, Harvard Medical School, Boston, MA, USA
4 The Proteomics Platform, The Broad Institute of MIT and Harvard, Cambridge, MA, USA
5 F.M. Kirby Neurobiology Center, Boston Children's Hospital, Boston, MA, USA
6 Howard Hughes Medical Institute, Boston Children's Hospital, Boston, MA, USA
7 Massachusetts General Hospital, Department of Psychiatry, Boston, MA, USA
8 Howard Hughes Medical Institute, Harvard Medical School, Boston, MA, USA
9 Currently: Vigil Neuroscience, Cambridge, MA, USA
10 Department of Brain and Cognitive Sciences, Massachusetts Institute of Technology, Cambridge, MA, USA
11 Equal Contributions
*Correspondence: msheng@broadinstitute.org, agranger@broadinstitute.org, bsong@broadinstitute.org

Abstract

Loss-of-function mutations in *AKAP11* (a protein kinase A (PKA)-binding protein) greatly increase the risk of bipolar disorder and schizophrenia. To determine the neurobiological functions of AKAP11 and the consequences of its absence, we conducted multi-omic analyses of *Akap11* mutant mouse brains. We find that AKAP11 is a key regulator of PKA proteostasis in the brain whose loss leads to dramatically elevated PKA expression and phosphorylation, especially in synapses. Transcriptomic analysis shows extensive gene expression changes throughout the brain, including prominent decreases in synapse-related genes sets. Gene expression is especially affected in spiny projection neurons of the striatum, a brain region implicated in motivation, cognition and psychiatric disorders. *In vivo*, real-time measurements of PKA activity in ventral striatum of *Akap11*$^{-/-}$ mice revealed constitutively elevated kinase activity, which distorts dopamine to PKA signaling. Our work reveals the molecular basis of circuit dysfunction in a genetically valid model of psychotic disorder.

Introduction

Bipolar disorder (BD) and schizophrenia (SCZ) are debilitating psychiatric conditions within the psychosis spectrum whose biological basis remains unknown. Bipolar disorder is typically characterized by episodes of mania alternating with periods depression. Schizophrenia is characterized by positive symptoms including hallucinations and delusions that occur alongside negative symptoms that include emotional impairment; and is often associated with cognitive

symptoms. Together, BD and SCZ account for a substantial fraction of the global mental health crisis: the lifetime prevalence of BD is 1-2%[1] and SCZ is approximately 0.7%[2]. Both diseases have substantial heritability (60-80%)[3,4], suggesting that gene-derived molecular programs contribute towards disease risk.

Recent landmark exome sequencing efforts have led to the discovery of several genes whose loss of function greatly increase the risk for schizophrenia (SCZ)[5] and bipolar disorder (BD)[6]. These rare variant mutations are associated with large odds ratios (3-50), conferring much more substantial risk than common variants previously identified by genome-wide association studies (<1.1)[7,8]. In further contrast to GWAS-associated loci, these mutations occur in coding sequences of specific genes and can be inferred to be loss of function in nature.

Mutations in *AKAP11* (A-kinase anchoring protein 11) are associated with greatly elevated risk of both SCZ and BD[5,6,9]. In a replication study accounting for diverse ancestries, *AKAP11* was validated as schizophrenia risk gene, reaching exome wide significance[9]. *AKAP11* has not been associated with autism spectrum disorder, epilepsy or intellectual disability[6] and therefore is a relatively specific risk gene for the SCZ-BD psychotic disorder spectrum. In contrast, previously studied large-effect SCZ risk variants[10–12] are also associated with intellectual disability and developmental disorders[5], making *Akap11* animal models particularly interesting to study. In our previous neurophysiologic study, we reported that *Akap11* loss-of-function mutant mice recapitulate several electroencephalogram (EEG) abnormalities found in schizophrenic patients, including increased power of resting gamma oscillations, non-rapid eye movement (REM) sleep reduction, and gene-dose-dependent reduction in sleep spindles[13]. The molecular, cellular and circuit mechanisms by which *Akap11* deficiency results in brain dysfunction has not been studied.

The *Akap11* gene encodes a member of the A-Kinase anchoring proteins (AKAPs), which bind Protein Kinase A (PKA) and are typically localized to compartments within a cell, targeting PKA to specific subcellular domains[14]. In non-neuronal cell lines, AKAP11 is reported to localize to punctate structures, including multivesicular bodies[15] and peroxisomes[16]. In addition to PKA, AKAP11 is reported to interact biochemically with the protein kinase GSK3β[17], Protein Phosphatase 1[18], IQGAP1[19], $GABA_C$ receptors[20], and vesicle-associated proteins A and B (VAPA, VAPB)[21], each of which is implicated in signaling and trafficking pathways that influence synaptic plasticity and neuronal development. Intriguingly, AKAP11 not only binds but inhibits the activity of GSK3β[17], a target of the mood-stabilizing drug lithium that is used to treat BD. AKAP11 also functions as an autophagy receptor for the regulatory subunit 1 of PKA (*Prkar1a*) which promotes protein-level degradation of PRKAR1α in the context of cellular stress[22]. Because AKAP11 has not been studied in the brain, there is insufficient knowledge to bridge the cell biology of *AKAP11* and psychiatric disease risk. In this study, we use unbiased multi-omic approaches to explore the consequences of *Akap11* loss-of-function across widespread brain regions and cell types, spanning several postnatal ages, within synaptic compartments, and in the context of dopaminergic signaling, followed by *in vivo* fiber photometry measurements of PKA activity. Our data uncover a fundamental role of *AKAP11* in synapse function and highlight

the striatum as a nexus of circuit dysfunction in a model of psychosis risk with human-genetics validity.

Results

Identifying the AKAP11 interactome in brain

Little is known about AKAP11 in the brain, so we characterized the protein interactome of AKAP11 by immunoprecipitation of AKAP11 from cortical extracts followed by mass spectrometry (coIP-MS, Figs. 1a,b, Extended Data Fig. 1a). Of the ~2000 proteins identified by mass spectrometry, 68 proteins were enriched ($P < 0.05$) in AKAP11 coIP from *Akap11* wild-type (WT) cerebral cortex versus coIP from negative control *Akap11*$^{-/-}$ (knockout) mice[23]; these were considered specific interactors of AKAP11 (Fig. 1c; Supplementary Table 2). This approach yielded putative AKAP11-associated proteins that were largely overlapping with those found by comparison of AKAP11 coIP vs control IgG coIP from WT brains (Extended Data Fig. 1b). Of the 68 proteins that were specifically associated with AKAP11 in the brain, only 7 were previously reported in cell lines or other tissues, including PKA subunits, GSK3β, and VAPA and VAPB (Fig. 1d)[17,21]. The biochemical association of AKAP11 with PKA catalytic and regulatory subunits and several other interactors (VAPA, VAPB, GSK3β, DRYK1A) was confirmed by coIP-immunoblot experiments (Figs. 1e-1j). AKAP11 did not associate with the cytoskeleton protein Vinculin, indicating specificity for the above results (Fig. 1e).

Figure 1

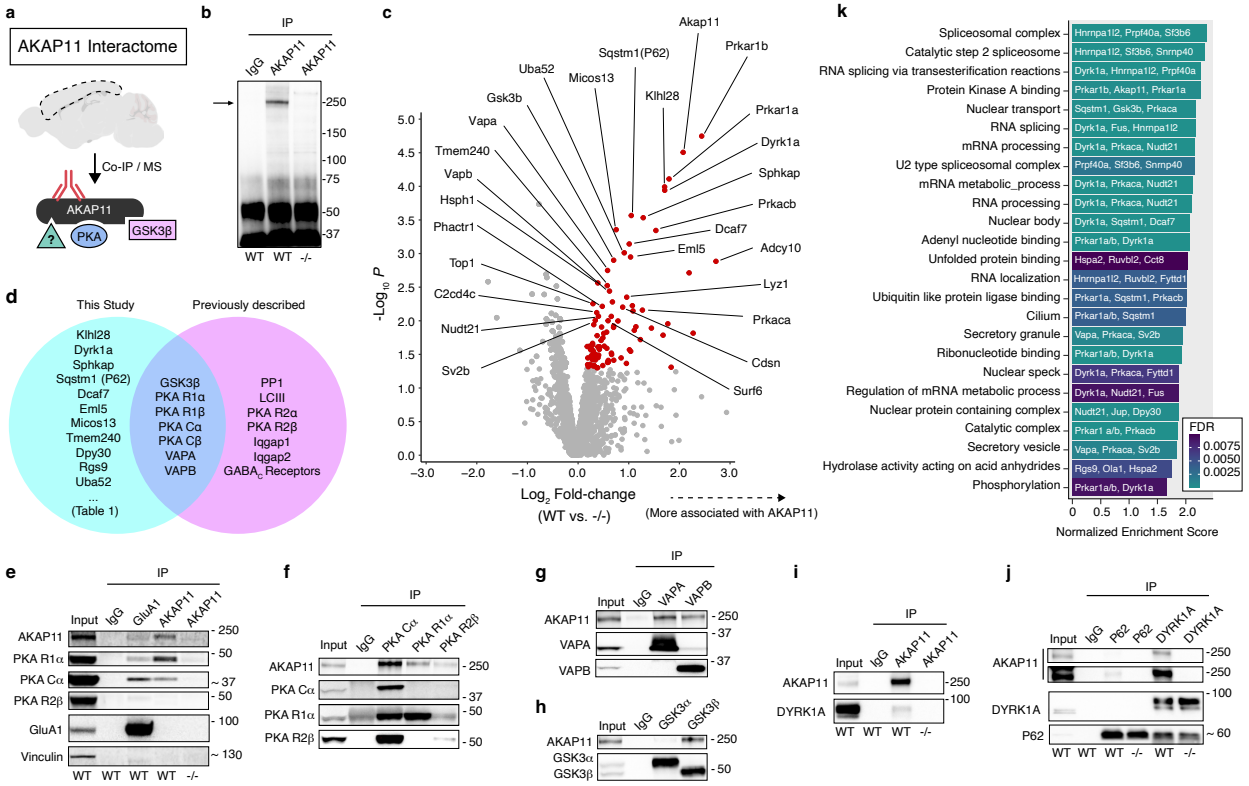

Figure 1: Characterization of the AKAP11 interactome in the brain.
a, Schematic of AKAP11 immunoprecipitation (IP) and its most notable, known interactors.
b, Immunoblot of AKAP11 in IPs of anti-AKAP11 and control IgG in 12-week-old (12wk) wild-type (WT) or *Akap11*$^{-/-}$ cortical tissue.
c, Volcano plot comparing Log_2 Fold-Change (Log_2FC) against *P* value for AKAP11 IP in WT vs *Akap11*$^{-/-}$, displaying all proteins detected by coIP-MS. Proteins that were enriched (red) by anti-AKAP11 IP from WT versus *Akap11*$^{-/-}$ cortical extracts. Enriched proteins, defined by having a nominal P value < 0.05 and $Log_2FC > 0$, are colored red. Downregulated proteins are mostly antibody-related artifacts and can be found in Supplementary Table 2).
d, Venn diagram comparing previously published AKAP11 interactions with the brain interactome in this study. Full results are displayed in Table S1.
e, Immunoblot of AKAP11, PKA subunits and control proteins, in IPs of AKAP11, GluA1 or IgG control in WT or *Akap11*$^{-/-}$ cortical lysate.
f, Immunoblot of AKAP11 in IPs of PKA subunits, in WT cortical lysates.
g-j, Immunoblot with indicated antibodies, in IPs of anti-GSK3α, GSK3β, VAPA, VAPB, AKAP11, P62 or DYRK1a in WT or *Akap11*$^{-/-}$ cortical lysate.
k, Gene set enrichment analysis of all proteins displayed in 1c, showing selected gene ontologies with a positive normalized enrichment score (NES) and adjusted *P*-value (FDR) < 0.01. Redundant (similar) pathways were removed for clarity. The top most enriched proteins within each ontology are listed within the histograms.

As expected for an AKAP protein[14], we observed high enrichment of multiple subunits of PKA in AKAP11 immunoprecipitates (Figs. 1c,e). PKA exists as a tetrameric holoenzyme with regulatory subunits that bind and suppress the kinase activity of catalytic subunits. In AKAP11 coIPs there was greater degree of enrichment for regulatory subunits PKA R1α and PKA R1β (encoded by *Prkar1a* and *Prkar1b*) than the catalytic subunits PKA Cα, PKA Cβ (encoded by *Prkaca* and *Prkacb*), which is consistent with AKAP11 directly binding to regulatory subunits of PKA[24]. Adenylyl cyclase 10 (encoded by *Adcy10*) was also enriched, and this enzyme produces cyclic AMP, which binds and activates PKA. There was only modest enrichment for type 2 regulatory subunits (PKA R2α, PKA R2β. Extended Data Fig. 1c) even though AKAP11 has high affinity binding sites for R2[24]. We confirmed that AKAP11 also associates with GSK3β in the brain, consistent with prior studies in cell lines[17,24,25] and did not detect an association with GSK3α (Fig. 1h).

Our coIP-MS experiments from brain uncovered multiple novel interactors of AKAP11 including DYRK1A, SPHKAP, Synaptic Vesicle Protein 2B (SV2B), and P62 (also known as SQSTM1) (Figs. 1c,d). By coIP-immunoblot, we confirmed AKAP11 binding to DYRK1A (Figs. 1i,j), a tyrosine kinase that is genetically linked to autism spectrum disorders[26] and is implicated in neurodevelopment, neurogenesis and neurite outgrowth[27–30]. Association with VAMP-associated Proteins A and B (VAPA/VAPB) and SPHKAP is suggestive of localization near endoplasmic reticulum (ER). VAPA/B are ER-resident proteins that facilitate inter-organelle contact and vesicular transport, and SPHKAP, which interacts with VAP proteins to regulate calcium signaling from ER stores[31]. We also explored the AKAP11 interactome by coIP from the brains of *Akap11*$^{+/-}$ (heterozygote) mutants, which mimics the human heterozygous genotype that is associated with greatly increased risk for SCZ/BD[6]. Proteins coIP'd with AKAP11 were largely similar in WT and *Akap11*$^{+/-}$ (Extended Data Figs. 1d,e).

To gain further insight into molecular pathways in which AKAP11 might play a role, we conducted gene-set enrichment analysis (GSEA)[32] on AKAP11-associated proteins (Fig. 1k,

155 Supplementary Table 3). In addition to expected gene ontology (GO) pathways like
156 “Phosphorylation”, we observed enrichment in AKAP11 coIP of the “Ubiquitin like protein ligase
157 binding” GO term, which includes the selective autophagy receptor P62 and RPL40 (encoded
158 by *Uba52*) (Extended Data Fig. 1f). In cell lines, AKAP11 interacts with autophagosomes,
159 intracellular vesicular structures involved in protein degradation[33], through the selective
160 autophagy receptor LC3[22,34]. In our coIP experiments, we found an association of AKAP11 with
161 P62, but not LC3 (Extended Data Fig. 1c), suggesting that in the brain, AKAP11 also interacts
162 with autophagosomes but possibly by distinct molecular mechanisms.

163 **Accumulated PKA in *Akap11* mutant mice**
164
165 Given our finding that AKAP11 could interact with autophagosomes, coupled with previous
166 studies showing its role in targeting proteins for degradation, we tested how interacting protein
167 abundance was altered by loss of AKAP11. By immunoblotting of total cortical lysate, we found
168 a striking elevation of PKA protein levels (regulatory (~6x) and catalytic (~9x) subunits in
169 *Akap11*$^{-/-}$ mice) (Fig. 2a, Extended Data Fig. 2a). The association of AKAP11 with P62 in the
170 brain (Fig. 1c) suggests the possibility that AKAP11 regulates degradation of PKA by receptor-
171 mediated selective autophagy. Levels of other AKAP11 interactors (GSK3β, VAPA/B, P62 and
172 DYRK1A) were not substantially altered in *Akap11* mutant brains.
173

Figure 2

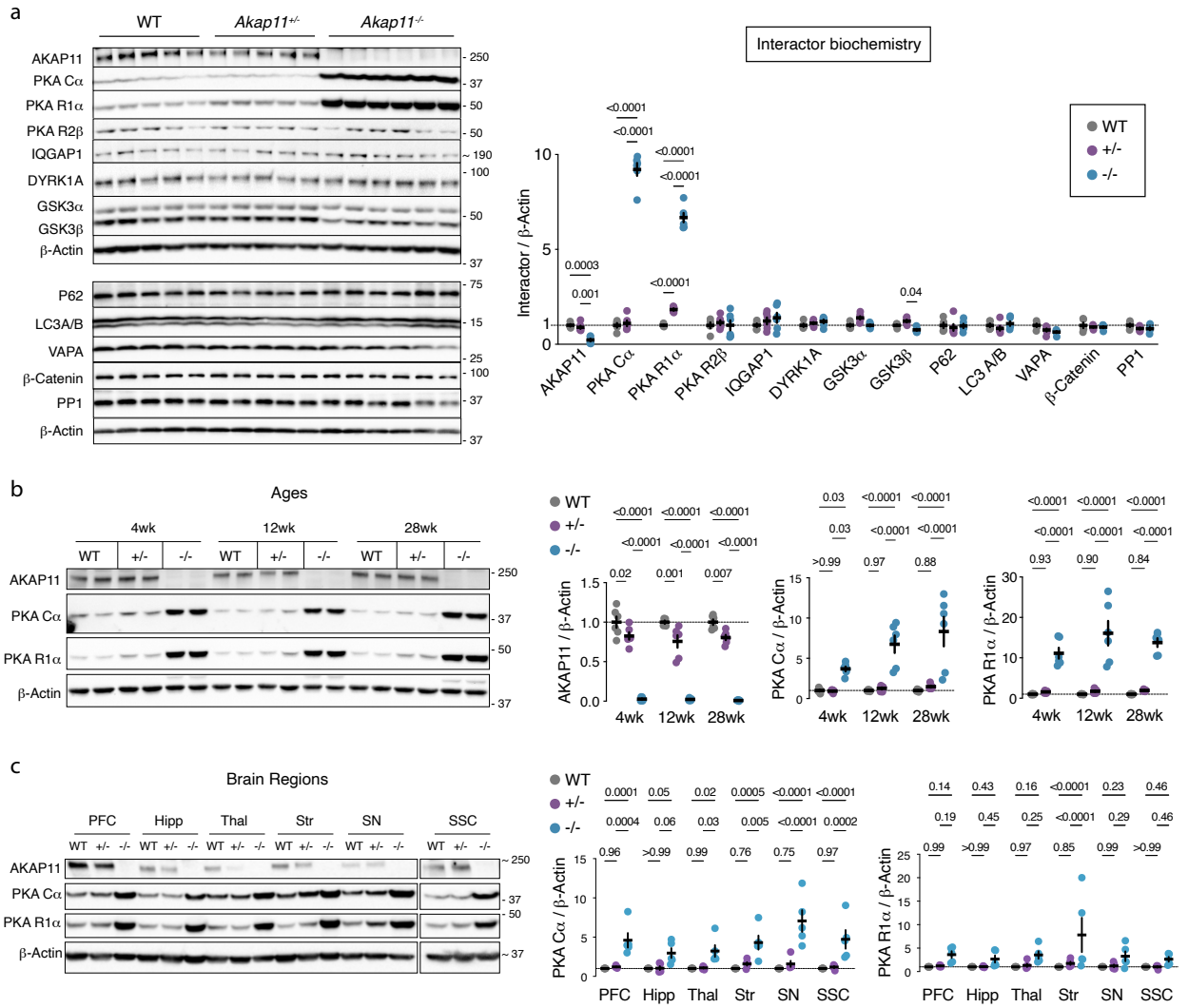

Figure 2. PKA protein levels are elevated across brain regions and ages of *Akap11* mutant mice.
a, Immunoblots and quantifications of 12wk cortex using antibodies against AKAP11-interacting proteins. Measurements are normalized to β-Actin and to WT controls for each antibody. $P < 0.05$ comparisons are shown.
b, Immunoblots and quantifications of 4wk, 12wk and 28wk cortex using antibodies against AKAP11 and PKA subunits. Measurements are normalized to β-Actin and to WT controls within an age group.
c, Immunoblots and quantifications from microdissected tissue from 4wk mice using antibodies against AKAP11 and PKA subunits. Measurements are normalized to β-Actin and to WT controls within a region.
a-c, Data are represented as mean +/- SEM. Two-way ANOVA with Tukey's post hoc test. See Supplementary Table 1 for exact *P*-values, statistical tests and sample sizes for each comparison.

The marked elevation of PKA subunits in *Akap11*$^{-/-}$ mice was apparent at all ages examined (4, 12, 28 weeks of age, Fig. 2b). PKA subunits were increased not only in the cortex, but across all brain regions examined: prefrontal cortex (PFC), somatosensory cortex (SSC), striatum (Str), hippocampus (Hipp), thalamus (Thal) and substantia nigra (SN) (Fig. 2c). Compared with the multiple-fold increases in the homozygous (*Akap11*$^{-/-}$) mutant, changes in PKA protein levels in the heterozygous (*Akap11*$^{+/-}$) mutant brain were much more modest (Figs. 2a-c). Nonetheless,

comparison with WT animals showed that PKA R1α and Cα subunits were consistently elevated by 20%-75% in *Akap11*$^{+/-}$ (Extended Data Figs. 2b,c). In the course of these immunoblotting experiments, we noted that levels of AKAP11 protein itself were reduced by much less than 50% in heterozygous (*Akap11*$^{+/-}$) mutants (Figs. 2a-c, Extended Data Figs. 2a-d), despite gene-dose dependent reduction of *Akap11* RNA (Extended Data Fig. 2e). This pattern is suggestive of posttranscriptional homeostatic compensation of *Akap11* expression when just one copy of the *Akap11* gene is deleted, and might explain the relatively modest effect on PKA in *Akap11*$^{+/-}$ vs. *Akap11*$^{-/-}$. Quantitative immunofluorescence imaging of PKA R1α protein in brain sections showed increased intensity across all brain regions of *Akap11*$^{-/-}$ mice (Extended Data Fig. 2f). Level of *PKA R1α* RNA was not significantly altered in *Akap11*$^{-/-}$ (Extended Data Fig. 2g), suggesting that AKAP11 regulates the stability or turnover of PKA at the protein level.

Synapse protein changes and elevated PKA in AKAP11 deficient mice

PKA plays a key role in regulation of synaptic plasticity[35]. To understand the consequences of *Akap11* deficiency and PKA elevation in synapses, we investigated protein changes in purified synaptic ("PSD (postsynaptic density)") fractions of *Akap11* mutant mice by quantitative mass spectrometry-based proteomics and phosphoproteomics using Tandem Mass Tag (TMT) labeling (see methods). Since the onset of SCZ occurs typically in adolescence and early adulthood[36], we examined 4 week (juvenile) and 12 week (young adult) mice. ~9000 proteins were identified in the PSD fraction purified from cortex, including AKAP11 itself which was modestly (~2x) enriched in the PSD fraction vs total lysate (Extended Data Figs. 3a,b). The number of differentially abundant proteins (DAPs, nominal $P < 0.05$) was greater in *Akap11*$^{-/-}$ than *Akap11*$^{+/-}$ mutants at 12 weeks but similar at 4 weeks, with approximately equal proportion of upregulated and downregulated DAPs overall (Fig. 3a, Supplementary Table 2). The DAPs were well correlated between *Akap11*$^{+/-}$ and *Akap11*$^{-/-}$ genotypes (Extended Data Fig. 3c) and weakly correlated between 4 and 12 weeks (Extended Data Fig. 3d).

In *Akap11*$^{-/-}$ synapses, the catalytic subunits PKA Cα and PKA Cβ were the two most upregulated proteins, at both 12 weeks (Fig. 3b) and 4 weeks, with PKA regulatory subunits upregulated to a lesser extent (Extended Data Figs. 3e,f). Immunoblotting confirmed strong accumulation of PKA Cα (~5x) and R1α subunits (~2-3x) in homozygous *Akap11*$^{-/-}$ PSD fractions (Fig. 3c) and modest elevation of PKA Cα (~1.3x -1.6x) in heterozygous *Akap11*$^{+/-}$ synapses (Extended Data Fig. 3g). Besides PKA, many proteins showed changes in *Akap11*$^{-/-}$ synapse proteomics. Levels of SIK2, a PKA-regulated kinase involved in mood and circadian rhythms[37] and ARHGAP20, a Rho GTPase-activating protein[38], were significantly decreased in *Akap11*$^{-/-}$ synapses, at both 4 weeks and 12 weeks (Fig. 3b, Extended Data Figs. 3e,f). Notably, levels of AKAP11 itself were significantly decreased in *Akap11*$^{+/-}$ synapse fractions (Figs. 3b,c; Extended Data Fig. 3e), which is in contrast to the minimally altered levels of AKAP11 in *Akap11*$^{+/-}$ crude lysate (Fig. 2; Extended Data Fig. 2). This suggests that AKAP11 haploinsufficiency results in synapse-specific alterations to cellular signaling that are not apparent in bulk tissue readouts.

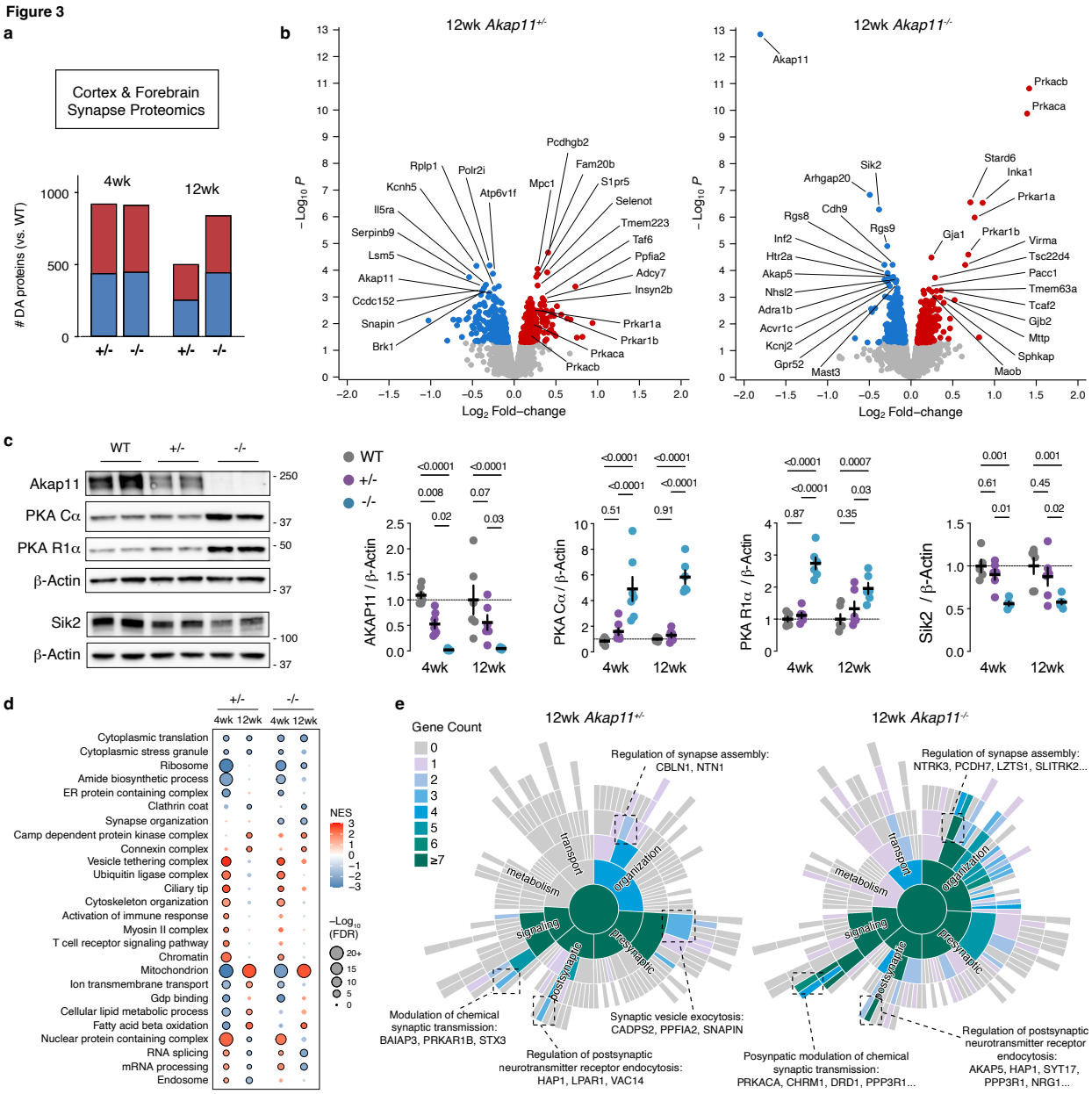

Figure 3: PKA accumulates in synapses of *Akap11* mutant mice

a, Number of DAPs across different ages and genotypes in synapse proteomics. Shading indicates upregulated (red) and downregulated (blue) DAPs, respectively. 4wk synapse proteomics data also appears in (Aryal et al., 2023)[39].

b, Volcano plots of 12wk synapse proteomics in *Akap11* mutants relative to WT. Upregulated and downregulated DAPs are colored red and blue, respectively.

c, Immunoblotting of synapse fractions with antibodies against AKAP11, PKA subunits, and SIK2. Right, quantifications for 4wk and 12wk animals. Data are represented as mean +/- SEM. Two-way ANOVA with Tukey's post hoc test. See Supplementary Table 1 for statistics.

d, A selection of GSEA analysis of synapse proteomics. Pathways displayed were significant at FDR < 0.05 in at least two age/ genotype conditions.

e, Sunburst plots showing SynGO Biological Process pathways and the number of $P < 0.05$ proteins within these ontologies. For selected ontologies, representative DAPs in the ontology are shown.

GSEA analysis of the synapse proteomic changes (Fig. 3D, Supplementary Table 3) revealed upregulation of “Vesicle tethering complex” and “Ubiquitin ligase complex” processes at 4 weeks (Fig. 3d, Extended Data Fig. 3h), which resembles the pathway changes observed in synapses purified from BD and SCZ human brain tissues[39]. These findings may relate to our observation that AKAP11 interacts with proteins involved in ER-Golgi transport and proteostasis (Figs. 1c,k). We further examined the precise ontologies of DAPs using SynGO[40] to dissect the “sub-synaptic” processes that are altered in *Akap11* mutant synapses (Fig. 3e). DAPs in *Akap11*$^{-/-}$ mutant synapses were represented among pathways such as “Postsynaptic modulation of chemical transmission”, and “Postsynaptic neurotransmitter receptor endocytosis”. Relatedly, proteins in the “Clathrin coat” gene ontology were downregulated in 4wk and 12wk Akap11$^{+/-}$ synapse proteomes (Extended Data Fig. 3i).

Hyperphosphorylation of synapse proteins in *Akap11* mutant mice

Within *Akap11*$^{-/-}$ synapses, the levels of several protein kinases and phosphatases were altered, most prominently the accumulation of PKA catalytic subunits Cα and Cβ (Fig. 3b,c, Extended Data Fig. 3e). To quantify phosphorylation changes in synaptic proteins in an unbiased fashion, we analyzed PSD fractions purified from *Akap11* mutant cortex by quantitative phosphoproteomics. *Akap11* mutants showed a large number of differentially abundant phosphoproteins (DAPPs, nominal $P < 0.05$), which was higher in *Akap11*$^{-/-}$ than *Akap11*$^{+/-}$, and higher at 4 weeks than 12 weeks (Fig. 4a, Extended Data Fig. 4a, Supplementary Table 2). We mapped changes in the synapse phosphoproteome against a reference of known and predicted kinase effectors[41] to infer the kinases responsible. The vast majority of PKA phospho-substrates detected in the synapse phosphoproteomics data were increased in abundance in *Akap11*$^{-/-}$ *;* and a number of these phosphoproteins were also highly upregulated in *Akap11*$^{+/-}$ heterozygous mutant synapses (Fig. 4b). The sequences flanking the phosphosites showed strong enrichment of the basophilic RRXS*/T* motif, particularly in the upregulated DAPPs of *Akap11*$^{-/-}$ synaptic fractions at both 4 and 12 weeks (Fig. 4C), which matches the consensus amino acid sequence that is preferred for phosphorylation by PKA[42]. Together, the synapse proteomics and phosphoproteomics data show that PKA kinase activity as well as protein levels are abnormally elevated in the synapses of *Akap11* mutant mice.

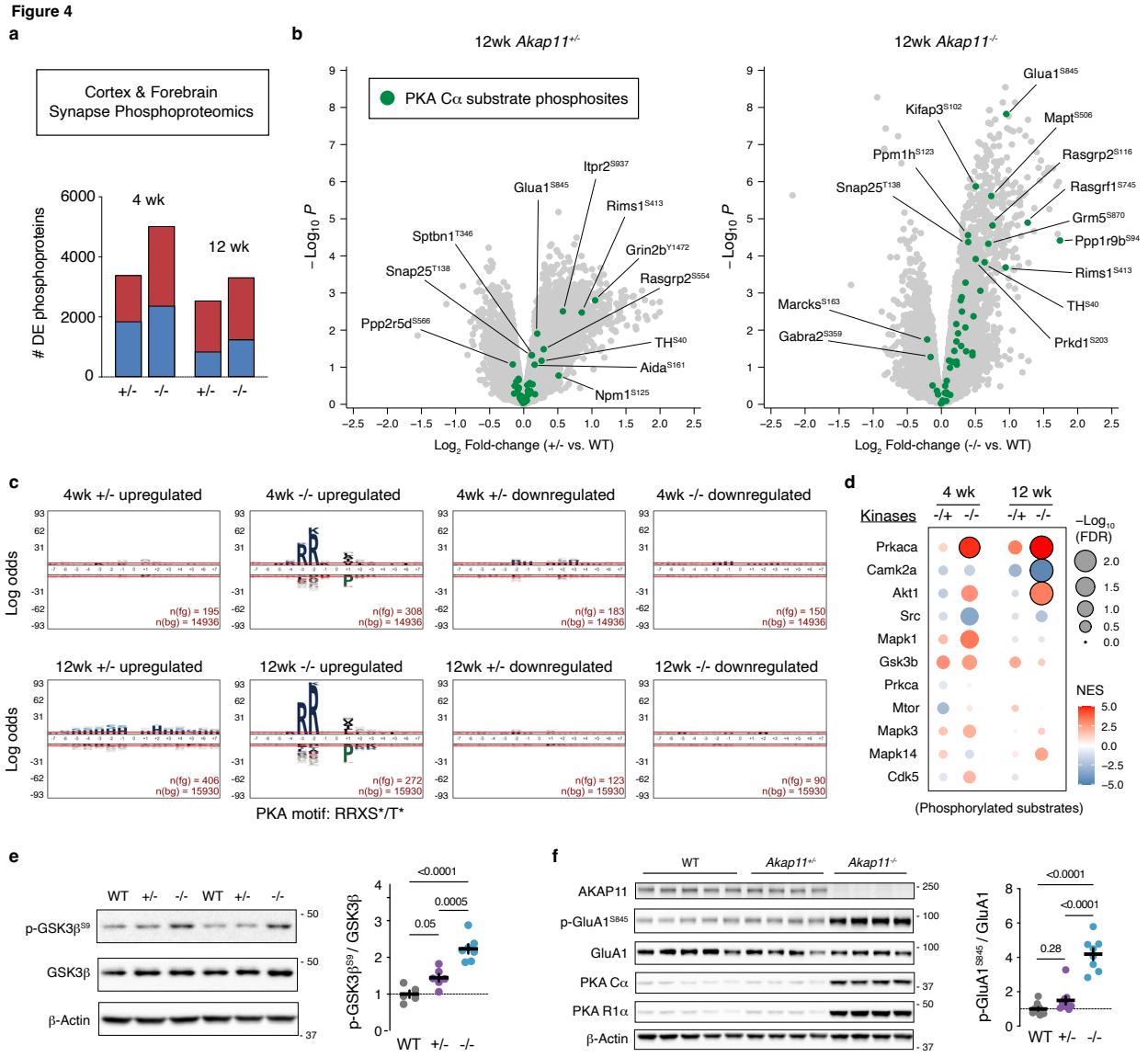

Figure 4: Phosphoproteomics of *Akap11* mutant synapses shows hyperphosphorylation of PKA substrates

a, Number of phosphoproteins reaching a significance threshold of nominal $P < 0.05$. Fractions of upregulated and downregulated DAPPs are highlighted in red and blue respectively.

b, Volcano plots of 12wk synapse phosphoproteomics data for *Akap11*$^{+/-}$ and *Akap11*$^{-/-}$ vs. WT controls. Phosphoproteomic measurements are normalized to MS-proteomics measurements from the same samples. Known PKA Cα substrates from PhosphoSitePlus are labeled green. AKAP11 phosphopeptides are omitted from *Akap11*$^{-/-}$ plots, for clarity.

c, Motif analysis of peptides flanking the phosphorylation site of $P<0.05$ phosphosites in A. n(fg) are the number of foreground peptides, and n(bg) are the number of background peptides. Red lines indicate FDR significance.

d, PTM-SEA of synapse phosphoproteomics data, using known kinase substrates from PhosphoSitePlus. Black borders indicate FDR significance.

e, Immunoblotting and quantification of p-GSK3β^{S9} and GSK3β in 4wk cortical lysate.

f, Immunoblotting and quantification of AKAP11, PKA subunits, p-GluA1^{S845} and GluA1 in 12wk cortical lysate.

e,f, Data are represented as mean +/- SEM. One-way ANOVA with Tukey's post hoc test. See Supplementary Table 1 for detailed statistical information.

294 Post-Translational Modification Signature Enrichment Analysis (PTM-SEA), which measures
295 enrichment of kinase substrate sets (akin to GSEA using GO terms)[43], also indicated elevation
296 of phosphorylated PKA substrates in A*kap11*$^{-/-}$, and to a lesser degree, *Akap11*$^{+/-}$ synapses (Fig.
297 4d). Phosphorylation of substrates by CaMK2A, a kinase involved in synaptic potentiation[44] was
298 significantly downregulated in *Akap11*$^{-/-}$ synapses at 12 weeks. Since AKAP11 is reported to
299 inhibit GSK3β, it was intriguing to find that phosphorylation of *β*-Catenin (a well-known GSK3β
300 substrate, encoded by *Ctnnb1*) was increased at Ser37 in *Akap11* mutants[45,46] (Extended Data
301 Fig. 4c). Phosphorylation of GSK3β itself on S9, a PKA phosphosite that regulates GSK3β
302 activity[47], was significantly elevated in *Akap11* mutants (Fig. 4e). Regulation of brain GSK3β by
303 *Akap11* is especially relevant because lithium, an inhibitor of GSK3, is a mainstay treatment of
304 BD[48] and GSK3β overactivity has been implicated in SCZ animal models[49].
305
306 Notably, among the most highly changed phosphoproteins in *Akap11*$^{-/-}$ synapses was AMPA
307 receptor subunit GluA1 (*Gria1*), which is phosphorylated by PKA at S845 (annotated as S863 in
308 the UniProt mouse reference; Figs. 4b,f; Extended Data Figs. 4a,b). Phosphorylation of GluA1
309 at S845 is a well-known correlate of AMPA receptor trafficking to the synapse[50–54]. We
310 confirmed by immunoblotting that GluA1^{S845} phosphorylation was sharply increased (~4x) in
311 brain lysates of *Akap11*$^{-/-}$ mutants, while total GluA1 protein showed little change (Fig. 4f,
312 Extended Data Fig. 4d). Additional DAPPs in *Akap11*$^{-/-}$ synapses that are known to be regulated
313 by PKA include Snap25^{T138}, a phosphosite required for presynaptic vesicular release[55] and
314 RIM1^{S413}, phosphorylation of which is induced during synaptic potentiation[56–58] (Fig. 4b). In
315 *Akap11*$^{+/-}$ synapses, PKA substrate DAPPs included RIMS1^{S413} and ITPR2^{S937}, a phosphosite
316 that regulates intracellular calcium release[59]. The strength of synaptic transmission is regulated
317 in large part by dynamic phosphorylation of synaptic proteins, including postsynaptic glutamate
318 receptors subunits such as GluA1[60]. By mapping our phosphoproteomics data onto the
319 phosphosites that are induced with chronic neuronal activation or silencing[60], we found that
320 many phosphosites associated with upscaling or downscaling of synaptic strength were also
321 highly changed in *Akap11* mutants (Extended Data Fig. 4d), reflecting potential changes in
322 synaptic function.
323
324 **Aberrant synaptic function in *Akap11* mutants**
325
326 To directly examine synaptic function and plasticity in *Akap11* mutants, we performed
327 electrophysiology recordings from acute hippocampal slices (6-8 week old mice). Under basal
328 conditions, the stimulation input/output relationships (stimulation of Schaffer collaterals to CA1)
329 of *Akap11*$^{-/-}$ mice were indistinguishable from WT (Extended Data Fig. 5a). The amplitude of
330 early long-term potentiation (LTP) induced by theta burst stimulation (TBS) was modestly but
331 significantly reduced in *Akap11*$^{-/-}$ mice (Extended Data Fig. 5b). We speculate this phenotype
332 could be due to partial occlusion of LTP by hyperphosphorylated GluA1 at S845[53,61,62]. *Akap11*$^{-/-}$
333 slices also showed heightened paired-pulse facilitation (Extended Data Fig. 5c), suggesting
334 reduced presynaptic release probability, which might relate to altered RIM1^{S413} and Snap25^{T138}
335 phosphorylation seen in the synapse phosphoproteomics (Fig. 4b). The electrophysiologic
336 phenotype in heterozygous *Akap11*$^{+/-}$ hippocampus was generally not significantly different from
337 WT, though there was a trend toward reduced magnitude of early LTP (Extended Data Fig. 5b).

338
339 **Altered synaptic genes and striatal circuits revealed by spatiotemporal transcriptomic**
340 **survey**
341
342 Beyond AKAP11's biochemical and cellular functions, what are the brain region and circuit-level
343 consequences of *Akap11* deficiency? *Akap11* mRNA is broadly expressed across the brain and
344 across postnatal development in wild-type mice (Extended Data Fig. 6a). We conducted bulk
345 RNA-seq on PFC, SSC, Str, Thal, Hipp, SN, as well as single-nucleus RNA sequencing
346 (snRNA-seq) on PFC and Str, at 4 weeks and 12 weeks (Fig. 5a, Extended Data Figs. 6b,c) to
347 query the circuits and molecular pathways that are impacted by *Akap11* loss of function. By bulk
348 RNA-seq, we found more differentially expressed genes (DEGs; defined as genes that changed
349 in either direction with FDR <0.05, Supplementary Table 4) in *Akap11*$^{-/-}$ than *Akap11*$^{+/-}$, and at 4
350 weeks than at 12 weeks of age (Fig. 5b). Based on DEG count, the most impacted regions in
351 *Akap11*$^{-/-}$ were striatum, thalamus and PFC, whereas thalamus was the most affected in
352 *Akap11*$^{+/-}$. The striatum had by far the most DEGs, at either age, in *Akap11*$^{-/-}$. Only a few DEGs
353 were common across brain regions (Extended Data Fig. 6d), and the correlation of Log_2-Fold-
354 Changes of nominally significant genes was low between different brain regions, and modest
355 between 4 and 12 weeks for the same brain region (Extended Data Fig. 6e). Thus the
356 transcriptional consequence of *Akap11* mutation varies with the brain region and developmental
357 context.

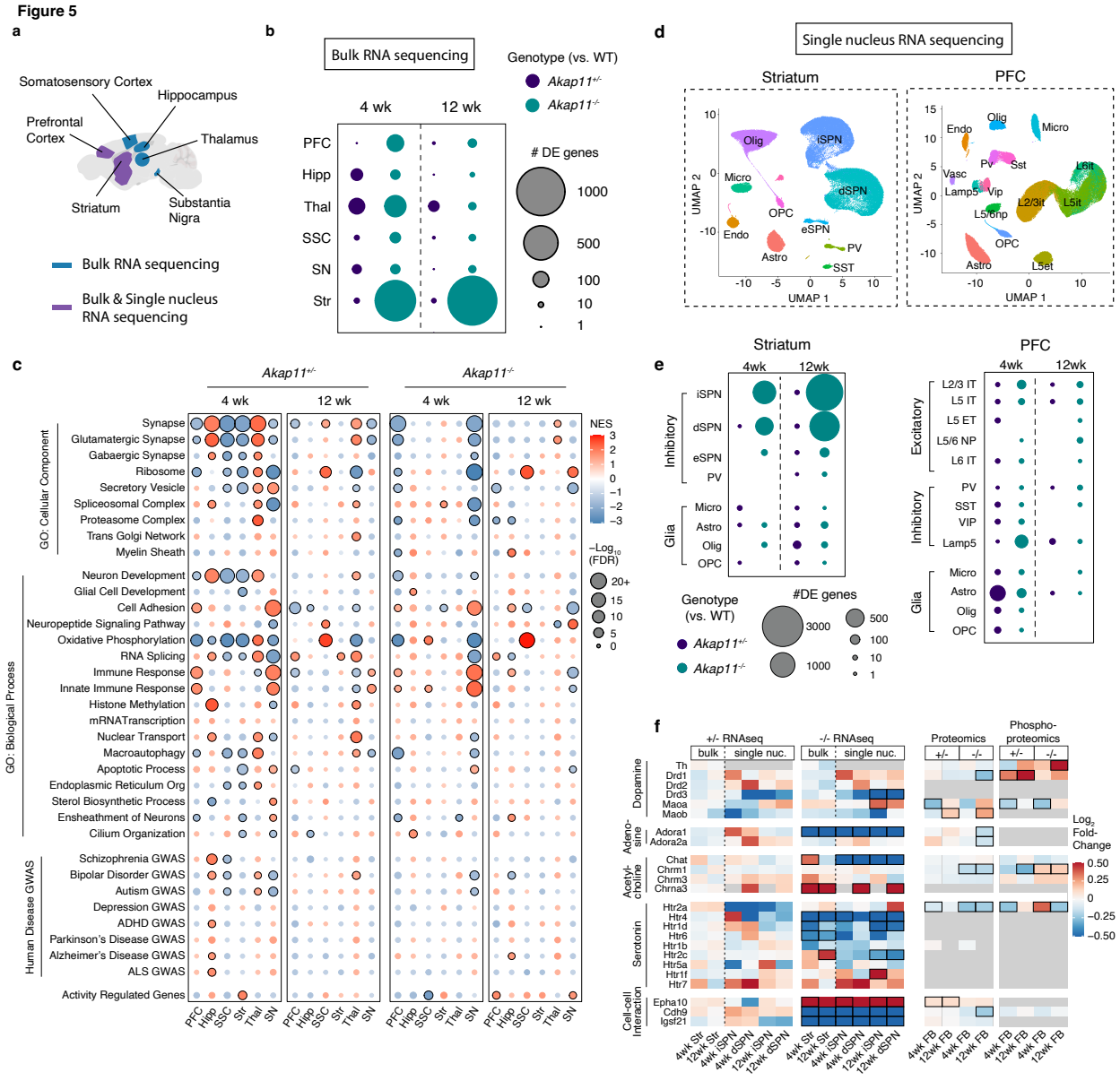

Figure 5: Transcriptome-wide impact of *Akap11* deficiency across ages, brain regions and cell types.
a, Schematic of brain regions collected for RNA sequencing.
b, Number of differentially expressed genes (DEGs) in bulk RNA sequencing across brain regions and ages. Experiments are n= 4 to 6 per condition (see Methods). Area of circles represents DEG counts, defined by FDR adjusted *P*-values < 0.05, for *Akap11* mutants compared to WT controls.
c, GSEA of bulk RNA sequencing, showing MsigDB pathways of interest, genes associated with psychiatric and neurological conditions by GWAS[11,71], and a curated set of activity-regulated genes[70]. Black outline indicates FDR < 0.05 significance.
d, Schematic of snRNA-seq experiments in PFC and striatum, with UMAP plots of major cell types identified at 12w by snRNA-seq. Experiments are n= 4 per condition, with the exception of 12w Str, with n=5 WT.
e, Number of DEGs in snRNA-seq experiments, defined by having an FDR adjusted *P*-value < 0.05.
f, Heatmap showing Log_2FC values for a selection of neuromodulation-related genes, plotted across transcriptomics, proteomics, and phosphoproteomics measurements. Genes indicated in the phosphoproteomics columns reflect the most significantly changed phosphosite per gene. *P* < 0.05 proteins and FDR < 0.05 transcripts are outlined with a black box.

374 GSEA of bulk transcriptomic changes revealed major dysregulation of biological pathways
375 related to synapses, mitochondria/oxidative phosphorylation, ribosomes, and RNA
376 processing/splicing, which was particularly evident in 4wk *Akap11*$^{+/-}$ (Fig. 5c, Supplementary
377 Table 5). The "Synapse" GO term was consistently downregulated in PFC and SN at both 4 and
378 12 weeks in *Akap11*$^{+/-}$ and *Akap11*$^{-/-}$ mutants (Fig. 5c). Immune-related pathways were
379 upregulated in the 4wk PFC and SN, which is notable in the context of synaptic pruning by glia
380 during development and disease[63] and SCZ patient associations with immune-related genetic
381 loci[64,65]. Two pathways required for cellular energetics and upkeep, "Oxidative phosphorylation"
382 (Ox-phos) and "Ribosome", were highly correlated, consistent with observations in another SCZ
383 rare variant mouse model *(GRIN2A)*[11]; these pathways are also altered in human SCZ
384 postmortem samples[66,67]. The "ribosome" and "oxidative phosphorylation" pathway, a
385 mitochondrial process that generates ATP for cells, was down in the PFC of 4 week *Akap11*$^{+/-}$
386 *and Akap11*$^{-/-}$ mutants (Fig. 5c). We investigated changes to neuronal activity, at the brain
387 region level in *Akap11* mutant mice. As a surrogate measure of neuronal activity, we conducted
388 GSEA of the bulk RNA-seq data using a set of activity-regulated genes (ARGs, Fig. 5c)[11,70]. At 4
389 weeks, ARGs were upregulated in the striatum of *Akap11*$^{+/-}$ and downregulated in the SSC and
390 PFC of A*kap11*$^{-/-}$ (though the latter did not reach significance). The consistent downregulation of
391 the "Synapse", "Ox-phos" and "ARGs" GO terms in PFC, is suggestive of selective hypofunction
392 of PFC that is reported in fMRI studies of humans with SCZ and BD[68,69].
393
394 We queried the bulk RNA-seq changes in *Akap11* mutants for enrichment of SCZ- and BD-
395 associated risk genes identified from human genome-wide association studies (GWAS) (Fig.
396 5c). The most significant enrichments were for BD risk genes, and interestingly, showed most
397 enrichment of these genes in *Akap11*$^{+/-}$ heterozygous mutants at 4 weeks (Fig. 5c). Though
398 reaching significance across fewer brain regions, the pattern of SCZ risk gene enrichment had
399 an overall similar pattern to BD. Besides SCZ and BD, we also observed similar GSEA signals
400 for genes associated with ASD and neurodevelopmental disorders[26,71–73]. Overall, these results
401 support that Akap11 functionally engages with other SCZ and BD and neurodevelopmental risk
402 genes, and are consistent with the known genetic overlap between SCZ, BD, and
403 neurodevelopmental disorders (NDD)[5,74].
404
405 **Major disturbances to striatal neurons revealed by single nucleus RNA-seq**
406
407 In WT mice, *Akap11* mRNA is expressed in excitatory and inhibitory neurons in all brain regions,
408 as well as in glia (Extended Data Fig. 7a). To investigate the cell type-specific effects of *Akap11*
409 deficiency, we conducted single-nucleus RNA sequencing (snRNA-Seq) in the PFC and
410 striatum at 4 and 12 weeks (Fig. 5d, Extended Data Fig. 7b, Supplementary Table 6). There
411 were no major changes in cell type proportions in *Akap11* mutant PFC or striatum (Extended
412 Data Fig. 6a). Though all cell types in PFC and striatum showed transcriptomic changes in
413 *Akap11* mutants the largest numbers of DEGs (FDR < 0.05) were found in the major neuron-
414 types of the striatum of *Akap11*$^{-/-}$, namely the inhibitory direct- and indirect-pathway spiny
415 projection neurons (dSPNs, iSPNs; Fig. 5e). Transcriptomic alterations in *Akap11*$^{-/-}$ mutants
416 were highly correlated between iSPNs and dSPNs (Extended Data Fig. 7c,d) and between 4
417 and 12 weeks of age (Extended Data Fig. 7d,e). Consistent with bulk RNA-seq findings (Fig.

418 5b), *Akap11*$^{+/-}$ had much less effect than *Akap11*$^{-/-}$ on SPN in snRNA-seq (Fig. 5e, Extended
419 Data Fig. 7d,f). Nearly all PFC neuron subtypes showed downregulation of the "Synapse" GO
420 term (Extended Data Fig. 8a, Supplementary Table 7), which aligns with bulk RNA-seq (Fig. 5c).
421 Unlike striatal neurons, which are much more impacted by homozygous *Akap11* mutation, glia
422 in the PFC and striatum (astrocytes, oligodendrocytes and microglia) showed comparable
423 numbers of DEGs genes between *Akap11*$^{+/-}$ and *Akap11*$^{-/-}$ (Fig. 5e). *Akap11* mutant astrocytes
424 showed downregulation of the "Sterol Biosynthesis" pathway, particularly in the 4 week
425 *Akap11*$^{+/-}$ PFC and *Akap11*$^{-/-}$ striatum (Extended Data Fig. 8b). Across regions, ages and
426 genotypes, decreases in synapse-related gene expression in neurons often occurred alongside
427 decreased expression of cholesterol biosynthesis genes in astrocytes (Extended Data Fig. 8c),
428 suggesting disturbed neuron-glia gene expression programs, as has been observed in
429 postmortem human SCZ brain tissue[75].
430
431 The largest changes in the *Akap11* mutant SPNs highlighted several neuromodulatory systems,
432 such as serotonin (*Htr2a*, *Htr4*), adenosine (*Adora1*), acetylcholine (*Chat*, *Chrna3*), and
433 dopamine (*Cartpt*) (Fig. 5f; Extended Data Fig. 9a,b). Intriguingly, the serotonin receptor
434 HTR2A, which is a target of hallucinogenic drugs[76,77], was downregulated in both *Akap11*$^{+/-}$
435 synapse proteomics and snRNA-seq of striatum SPNs, and Htr4 was robustly downregulated in
436 bulk RNA-seq of striatum and in snRNA-seq of striatal SPNs (Fig. 5f; Extended Data Fig. 9a,b).
437 Adenosine receptor ADORA1, a G-protein coupled receptor that inhibits cAMP production, was
438 downregulated in *Akap11*$^{-/-}$ synapse proteomics as well as in bulk RNA-seq and snRNA-seq
439 data in striatum and SPNs. Choline acetyltransferase (*Chat*) was also prominently
440 downregulated in the striatum of *Akap11*$^{-/-}$ (Fig. 5f). *Chat* participates in the synthesis of
441 acetylcholine, and signaling through muscarinic acetylcholine receptors is implicated in SCZ
442 pathophysiology[78,79]. Transcellular signaling factors *Epha10*, *Cdh9*, and *Igsf21* were among the
443 most altered genes in the *Akap11*$^{-/-}$ striatum (Fig. 5f). *Epha10* is a receptor tyrosine kinase that
444 acts as an axon guidance molecule[80,81]. *Cdh9,* which decreased consistently across proteomics
445 and transcriptomics measurements of *Akap11*$^{-/-}$, is involved in calcium dependent cell-cell
446 adhesion[82]. Together, these alterations in neuromodulation and trans-cellular signaling indicate
447 potentially aberrant cell-to-cell interactions in the striatum of *Akap11*$^{-/-}$ mice.
448
449 Dopamine is a key neuromodulator in the striatum[83]. Excessive or aberrant dopaminergic
450 signaling in the striatum is a long-standing hypothesis in pathophysiology of schizophrenia and
451 other psychiatric disorders, underpinned by the antipsychotic efficacy of D2 dopamine receptor
452 antagonists[84] .We found several dopamine-related genes, proteins, and posttranslational
453 modifications that were altered in *Akap11* mutants (Fig. 5f), including: (i) increased
454 phosphorylation of tyrosine hydroxylase (TH) at S40, which positively regulates its dopamine
455 biosynthesis activity[85,86]; (ii) reduction of protein and increased phosphorylation of dopamine
456 receptor DRD1, (iii) increased phosphorylation of RASGRP2^{S116} in 12 week *Akap11*$^{-/-}$ synapses
457 (Fig. 4b), which is consistent with enhanced DRD1 signaling[87] (iv) elevated MAO-B protein in
458 synapse fractions, an enzyme that degrades dopamine, v) increased proportion of Drd2-
459 *expressing* (Drd2^{+}) neurons in *Akap11*$^{+/-}$ relative to wild-type at 4 and 12 weeks (Extended Data
460 Fig. 9c). One dopamine-regulated transcript, *Cart* (Cocaine- and amphetamine-regulated
461 transcript)[88,89] was highly elevated in the *Akap11*$^{-/-}$ striatum (bulk RNA-seq) and in striatal SPNs

462 and PFC excitatory neurons (snRNA-seq) (Extended Data Fig. 9d) which may reflect altered
463 dopamine signaling in striatum and in PFC of *Akap11* mutants.
464
465 ***In vivo* striatal PKA dynamics and dopamine signaling are regulated by AKAP11**
466
467 The two most striking phenotypes of *Akap11* mutant mice are highly elevated PKA protein (Figs.
468 2-4) and strong transcriptomic changes in the striatum and SPNs (Fig. 5). PKA has outsized
469 importance in the striatum, acting in the signal transduction pathway downstream of dopamine
470 receptors[83]. To assess real-time dynamics of PKA activity in live animals, we used fluorescent
471 lifetime fiber photometry measurements of FLIM-AKAR, a fluorescent lifetime reporter of PKA
472 activity[90,91] that was virally expressed in the nucleus accumbens (NAc; within the ventral
473 striatum) (Fig. 6a, Extended Data Figs. 10a,b). In awake, behaving mice, PKA activity of
474 *Akap11*$^{-/-}$ mice was elevated across 10 minute recording sessions in an open field arena, (Fig.
475 6b) which was consistent across weeks of measurement (Extended Data Fig. 10c). As a
476 negative control, there were no differences across *Akap11* genotypes in the lifetime of FLIM-
477 AKAR^{T391A}, a mutated variant of FLIM-AKAR that is insensitive to PKA activity (Fig. 6c).
478

Figure 6

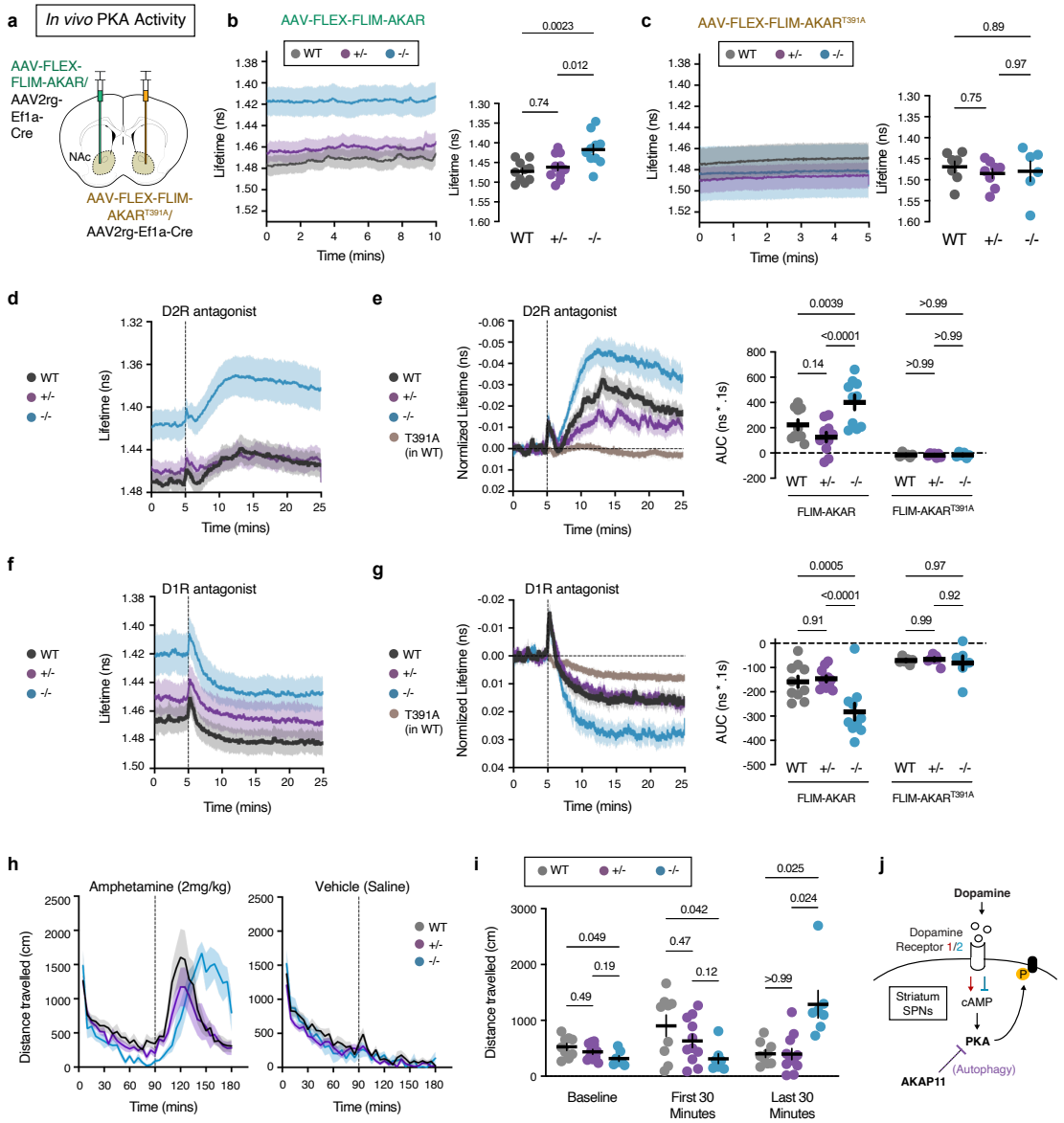

Figure 6: Fluorescence lifetime photometry (FLiP) in *Akap11* mutant mice reveals constitutively elevated PKA activity and functional alterations to striatal circuitry.

a, Schematic overview of the viral injection strategy.

b, Fluorescence lifetime of FLIM-AKAR in WT or *Akap11* mutant mice. The y-axis is inverted to reflect that decreased fluorescence lifetime corresponds to increased net PKA activity.

c, Fluorescence lifetime of FLIM-AKAR^{T391A} in WT or *Akap11* mutant mice.

d, Fluorescence lifetime changes of FLIM-AKAR in response to D2R antagonist.

e, Fluorescence lifetime changes of FLIM-AKAR in response to D2R antagonist, normalized to each genotype's baseline level of activity.

f, Fluorescence lifetime changes of FLIM-AKAR in response to D1R antagonist.

g, Fluorescence lifetime changes of FLIM-AKAR in response to D1R antagonist, normalized to each genotype's baseline level of activity.

h, Distance traveled after administration of amphetamine (2 mg/kg) or saline to WT or *Akap11* mutants.

i, Quantification of distance traveled during baseline (0-90mins), 90-120mins, and 150-180mins. Repeated measures two-way ANOVA with Tukey's post hoc test.

j, Schematic of dopamine → PKA regulation by *Akap11*.
b-i, Data are represented as mean +/- SEM, with the shaded regions or error bars representing SEM.
b,d,e,g, Two-way ANOVA with Tukey's post hoc test. See Supplementary Table 1 for statistics.

Dopamine receptors are enriched in the striatum, and excessive dopamine signaling in striatum may drive positive symptoms (e.g. hallucinations) of SCZ[92–94], which is supported by the clinical efficacy of dopamine receptor 2 (*Drd2*) antagonists for positive symptoms[84]. To evaluate how PKA is dynamically regulated by dopamine in *Akap11* mutants, we administered dopamine receptor antagonists via intraperitoneal injection. Dopamine acting on D2-type receptors inhibits cAMP production and thereby inhibits PKA[83,95]. As expected, PKA activity was increased in striatal neurons following D2 antagonist (eticlopride hydrochloride, 0.5 mg kg^{-1}) (Fig. 6d). Despite the higher levels of baseline PKA activity in *Akap11*$^{-/-}$ striatum, the magnitude of PKA stimulation (fold-increase of PKA activity) by D2 was further potentiated by *Akap11* deficiency (Fig. 6e). Dopamine acting on D1-type receptors stimulates cAMP synthesis and activates PKA[83,95]. Accordingly, administration of D1 antagonist (SKF83566, 3 mg kg^{-1}) suppressed PKA activity (Fig. 6f). If PKA activity is normalized to the pre-drug baseline level (Fig. 6g), D1R caused a more pronounced PKA inhibition in *Akap11*$^{-/-}$ mice. Thus loss of *Akap11* results in markedly higher basal PKA activity; however, this increased basal activity does not occlude further activation or block inhibition of PKA by dopamine receptor drugs, but rather expands the dynamic range of PKA activation or inhibition by dopamine.

Dopamine in the striatum regulates multiple aspects of behavior and cognition, including movement, reward processing and mood[96]. Dopamine levels induced by amphetamine are higher in the striatum of schizophrenic patients[97]. We tested locomotor response to subcutaneous amphetamine administration, which depends on dopamine and is often used as a behavioral measure of dopamine sensitivity in rodents (Figs. 6h,i). Wild-type mice, as expected, showed amphetamine-induced hyperactivity (AIH; measured by distance traveled). During the first 30 minutes after amphetamine administration, *Akap11*$^{-/-}$ mice displayed less AIH than WT littermates; however, *Akap11*$^{-/-}$ mice showed a much more sustained hyperactivity response, such that at 60-90 minutes after amphetamine administration, *Akap11*$^{-/-}$ mice still showed high levels of locomotion, when WT animals had returned to baseline (Fig. 6h). Together, these pharmacological manipulations, in conjunction with imaging and behavioral readouts, suggest that the temporal dynamics and strength of SPN signaling are distorted by elevated PKA activity in *Akap11* mutants (Fig. 6j).

Discussion

Genetic variation contributes substantially towards schizophrenia and bipolar disorder risk. Psychiatric symptoms ultimately emerge from dysfunction of specific neural circuits; however the cascade of events spanning from genetic to molecular-cellular to circuit dysfunction remain unclear. In this study, we examined mice deficient in *Akap11*, a shared risk gene for schizophrenia and bipolar disorder. Our unbiased multi-omic profiling of mutant mice led to key insights about *Akap11*'s role in the brain: 1) AKAP11 is a critical regulator of PKA protein levels;

538 its absence results in a remarkable elevation of PKA activity in synapses. 2) The striatum, the
539 major site of dopaminergic signaling and integration in the brain, is particularly impacted by
540 *Akap11* deficiency.
541
542 Our study brings attention to altered signaling factors downstream of dopamine --namely, PKA
543 misregulation in SPNs --as another mechanism that can disturb striatal dopaminergic signaling.
544 PKA is elevated across the brain in Akap11 mutants, so presumably, elevation of PKA activity
545 also contributes to pathological disturbance in other brain regions, cell types and circuits, such
546 as the PFC and thalamus, where we also saw major transcriptomic changes.

547 It is important to note that, in comparison with full *Akap11* knockout, the biological effects of
548 *Akap11* heterozygosity are relatively subtle. With the notable exception of thalamus and glia
549 (astrocytes, oligodendrocytes and microglia) transcriptomes, we observed much larger
550 phenotypes in homozygous mutants relative to heterozygotes. However, the phenotypes that
551 were most apparent in *Akap11*$^{-/-}$, such as elevated PKA, were also seen in *Akap11*$^{+/-}$ to a lesser
552 degree. Much of this modest effect could be explained by the tempered effect of *Akap11*
553 haploinsufficiency on AKAP11 protein levels, which may be more pronounced in specific
554 subcellular compartments (such as synapses) or environmental contexts. It would be interesting
555 to test whether cellular stressors, which can stimulate autophagy, could exacerbate the loss of
556 AKAP11 protein and amplify the elevation of PKA activity in *Akap11* heterozygous mutants,
557 thereby offering a potential way for environmental triggers to induce a disease phenotype.

558 There are likely to be hundreds of genetic variants underlying SCZ and BD. Because these
559 genes are diverse in nature and molecular function, their most proximal molecular mechanism
560 would be expected to be varied and perhaps unique to each genetic variant. Thus, it is essential
561 to identify downstream convergent cellular and circuit disturbances that are shared among
562 different risk genes. Our findings reveal one mechanistic pathway by which a specific genetic
563 variation leads to neural circuit dysfunction. In this case, loss of function of *Akap11*, which is
564 required for autophagy of PKA, leads to elevated PKA kinase activity in neurons, resulting in
565 unbalanced dopamine-to-PKA signaling in SPNs of striatum. Another mouse model of a rare
566 variant SCZ gene (*GRIN2A*)[5] also shows evidence of hyperdopaminergic signaling in striatum,
567 but via a mechanism different than exaggerated PKA activation[11]. In *SETD1A* and *Trio* loss of
568 function genetic models, which are also gene variants associated with greatly increased risk for
569 schizophrenia[5], elevated PKA activity has a causal role in synaptic dysfunction[12,98]. Further, the
570 cAMP synthesizing enzyme adenylyl cyclase 2 (*Adcy2*) is one of the most significant genetic
571 associations for bipolar disorder[8]. Thus, human genetics and mechanistic studies corroborate a
572 plausible role of PKA dysregulation in psychiatric disorders.

573 Our work, which started in unbiased omics fashion, highlights the fine molecular control of
574 striatal dopaminergic signaling–already much implicated in psychosis pathophysiology by
575 human and mouse model studies–as a worthy focus of future investigation. Our multi-omic
576 analysis of the *Akap11* mouse model, together with similar investigation of other high
577 penetrance SCZ and/or BD genes, should enable additional hypothesis-driven experiments and

lead to a more nuanced understanding of the complex and heterogeneous mechanisms underlying psychiatric disease.

603 **Supplementary Figure Legends and Tables**

Extended Data Figure 1

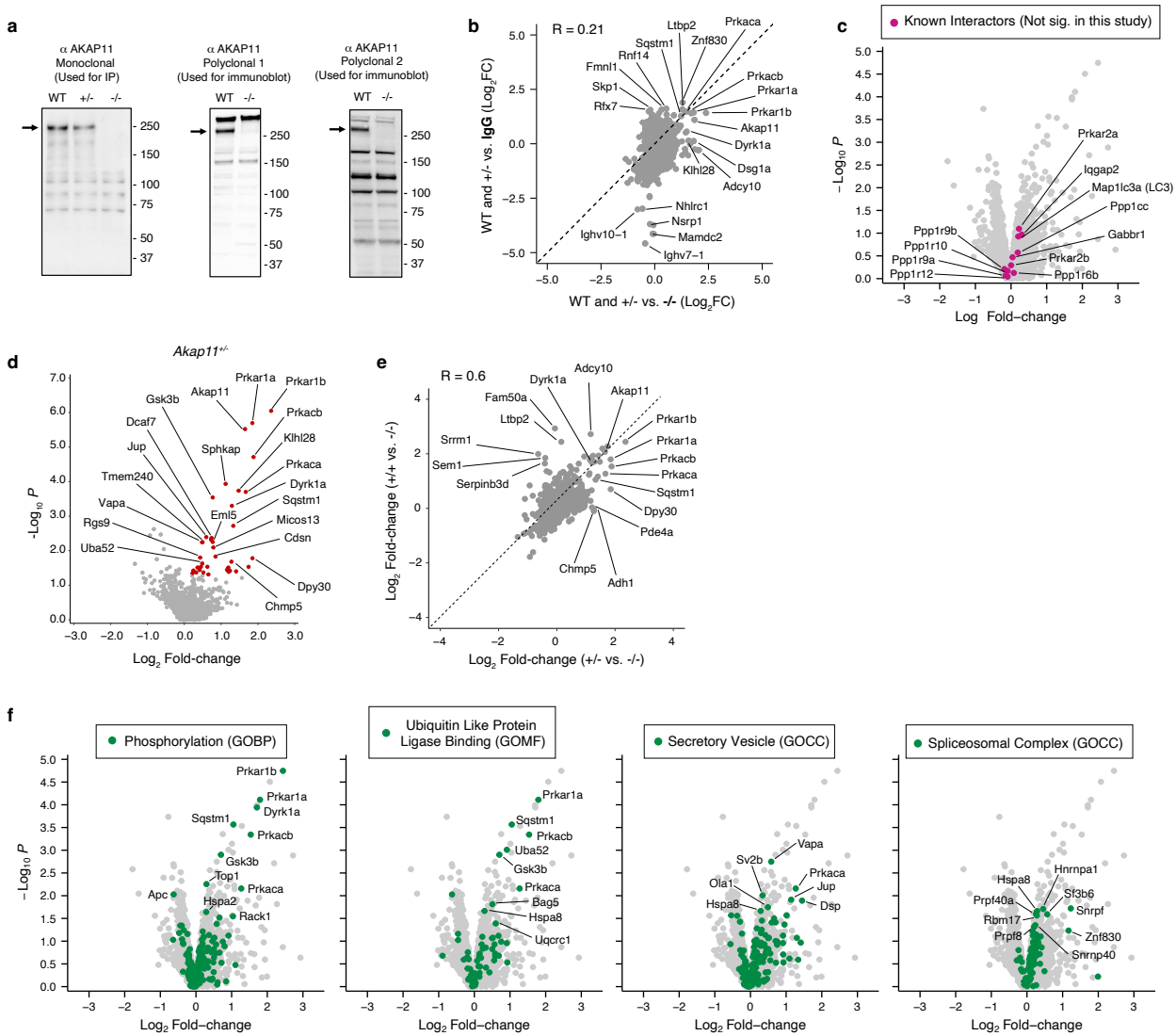

604
605 Extended Data Fig.1: AKAP11-interacting proteins and pathways in WT and in *Akap11*$^{+/-}$, related to Fig. 1.
606 **a,** Immunoblots of mouse cortex using AKAP11 antibodies used in this study.
607 **b,** Log_2FC scatterplot comparing *Akap11*$^{-/-}$ vs. IgG as controls for AKAP11 IP. In these data, AKAP11 IP in WT and
608 *Akap11*$^{+/-}$ animals were compared together against AKAP11 IP in *Akap11*$^{-/-}$ animals or IgG in WT animals.
609 **c,** Volcano plot of AKAP11 CoIP-MS (WT vs. *Akap11*$^{-/-}$). Highlighted in magenta are proteins that have been
610 previously reported to interact with AKAP11, but were not significantly enriched in this study.
611 **d,** Volcano plot of AKAP11 coIP-MS, comparing IP in *Akap11*$^{+/-}$ vs. *Akap11*$^{-/-}$ cortex. Proteins with nominal *P* value <
612 0.05 and $Log_2FC > 0$, are colored red.
613 **e,** Log_2FC scatterplots comparing all proteins detected by AKAP11 IP in WT versus *Akap11*$^{+/-}$.
614 **f,** Volcano plot of AKAP11 coIP-MS. Highlighted in green are proteins within gene ontology (GO) pathways that were
615 significantly found to be enriched by GSEA. (GOBP, Gene Ontology Biological Process; GOCC, Gene Ontology
616 Cellular Component; GOMF, Gene Ontology Molecular Function).
617 **b,e,** R = Pearson correlation.

Extended Data Figure 2

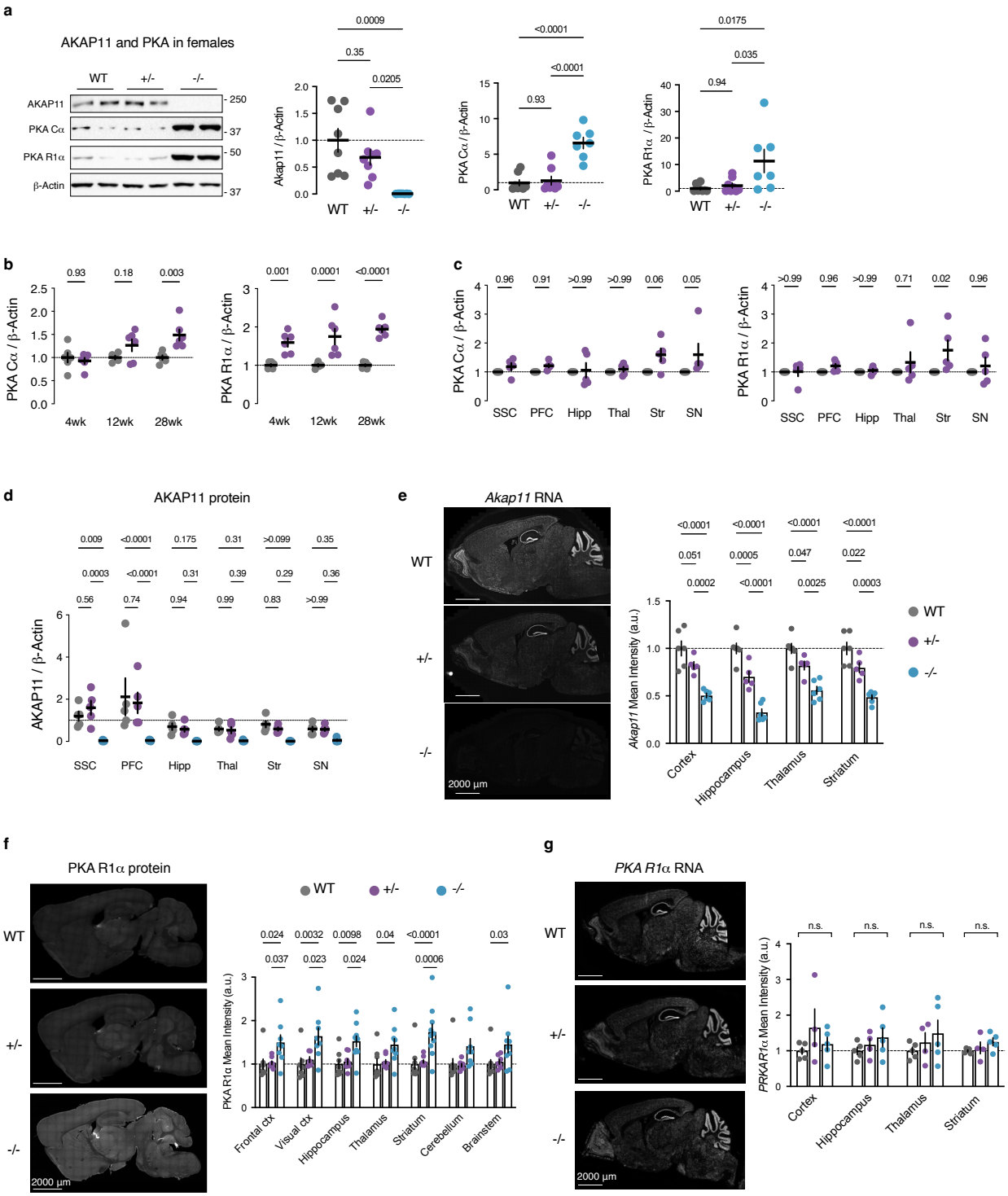

Extended Data Fig. 2. PKA protein levels in *Akap11*$^{+/-}$ and *in situ*, related to Fig. 2.
a, Quantifications of AKAP11 and PKA subunit protein levels in female 12wk WT and *Akap11*$^{+/-}$. One-way ANOVA with Tukey's post hoc test.

b,c, Quantifications of PKA subunit proteins levels in WT and *Akap11*$^{+/-}$. These data are also shown in Fig. 2b,c, but are rescaled here without *Akap11*$^{-/-}$ for clarity. Two-way ANOVA with Sidak's post hoc test.
d, Quantification of immunoblots from microdissected tissue from 4wk mice using antibodies against AKAP11. Representative immunoblots for these measurements are shown in Fig. 2c. *P*-values are calculated without *Akap11*$^{-/-}$ in multiple comparisons. Unlike other figures, these data are not normalized to WT within a brain region, in order to display differences in AKAP11 protein across brain regions.
e, *In situ* hybridization measurements of *Akap11* RNA. Right, quantification of mean intensity measurements within anatomical subregions. Measurements are normalized to WT controls within a region.
f, Immunofluorescence measurements of PKA R1α protein *in situ*. Right, quantification of mean PKA R1α immunofluorescence intensity measurements within anatomical subregions. Multiple comparisons adjusted *P* values < 0.05 are displayed above.
g, *In situ* hybridization measurements of *PKA R1α* RNA. Right, quantification of mean intensity measurements within anatomical subregions. Measurements are normalized to WT controls within a region.
d-g, Two-way ANOVA with Tukey's post hoc test. See Supplementary Table 1 for statistics.
a-g, Data are represented as mean +/- SEM.

Extended Data Figure 3

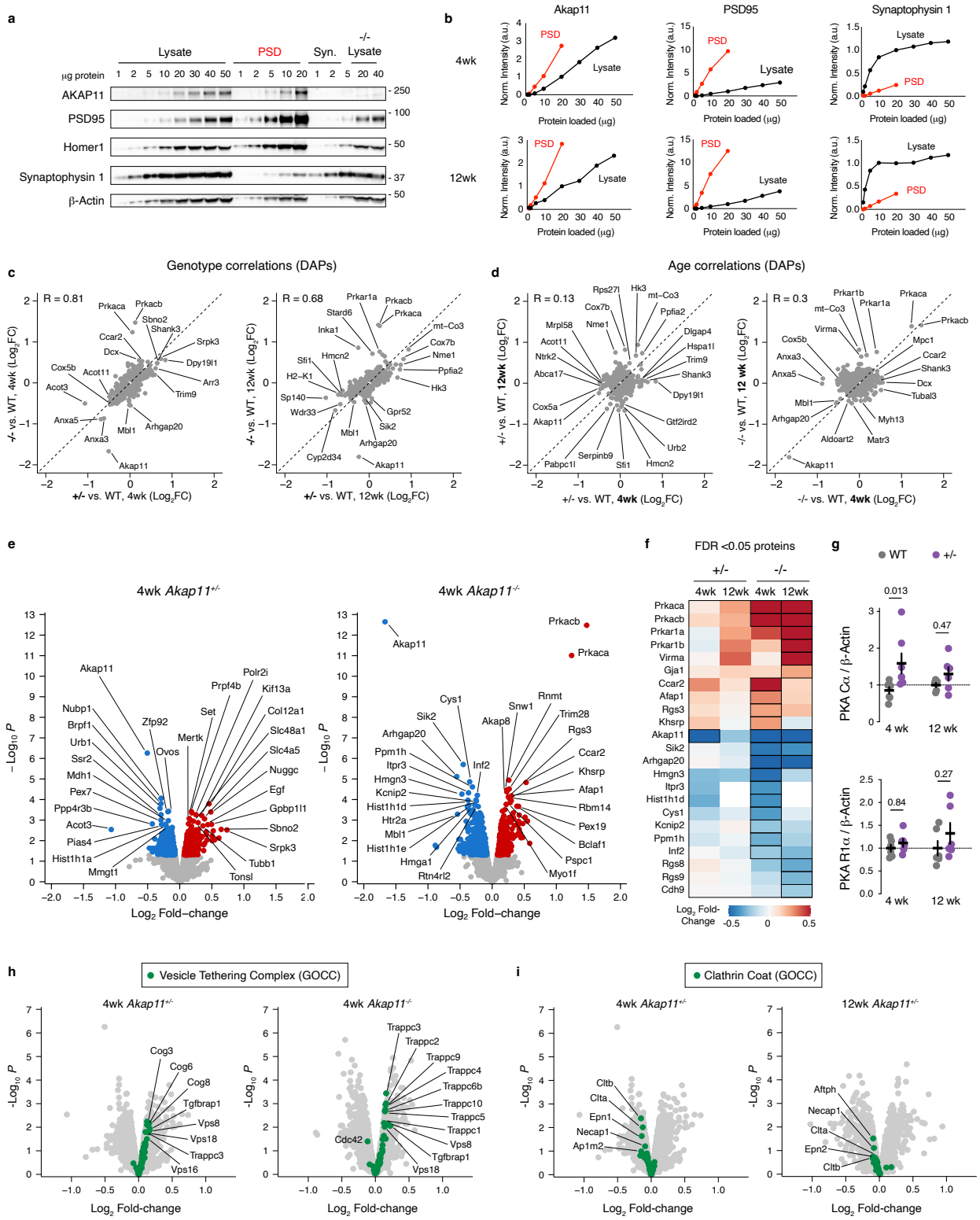

Extended Data Fig. 3. Comparisons of juvenile and adult synapse proteomes, related to Fig. 3.
a, Immunoblots of AKAP11 and synapse proteins across different amounts of lysate, synaptosome, and PSD-enriched fractions of 12wk cortex.

b, Quantifications of immunoblots in (a). Values are normalized to 20µg lysate.
c, Log_2FC scatter plots comparing DAPs in *Akap11*$^{+/-}$ vs. *Akap11*$^{-/-}$ synapse proteomes.
d, Log_2FC scatter plots comparing DAPs in 4wk vs. 12wk synapse proteomes.
e, Volcano plots of 4wk synapse proteomics data. Upregulated and downregulated DAPs are colored red and blue, respectively.
f, Heatmap of adjusted *P*-value (FDR) < 0.05 (black border) proteins across 4wk and 12wk synapse proteomes. Black border indicates FDR significance, including corrections for comparisons between *Akap11*$^{+/-}$ and *Akap11*$^{-/-}$.
g, Quantifications of PKA subunit proteins levels in WT and *Akap11*$^{+/-}$ synapses. These data are also shown in Fig. 3c, but are rescaled here without *Akap11*$^{-/-}$ for clarity. Data are represented as mean +/- SEM. Two-way ANOVA with Sidak's post hoc test. See Supplementary Table 1 for statistics.
h, Volcano plots of 4wk synapse proteomics data in *Akap11*$^{+/-}$. Proteins within the Vesicle Tethering Complex gene set are highlighted in green.
i, Volcano plots of synapse proteomics data in *Akap11*$^{+/-}$. Proteins within the "Clathrin Coat" gene set are highlighted in green for 4wk and 12wk animals.

Extended Data Figure 4

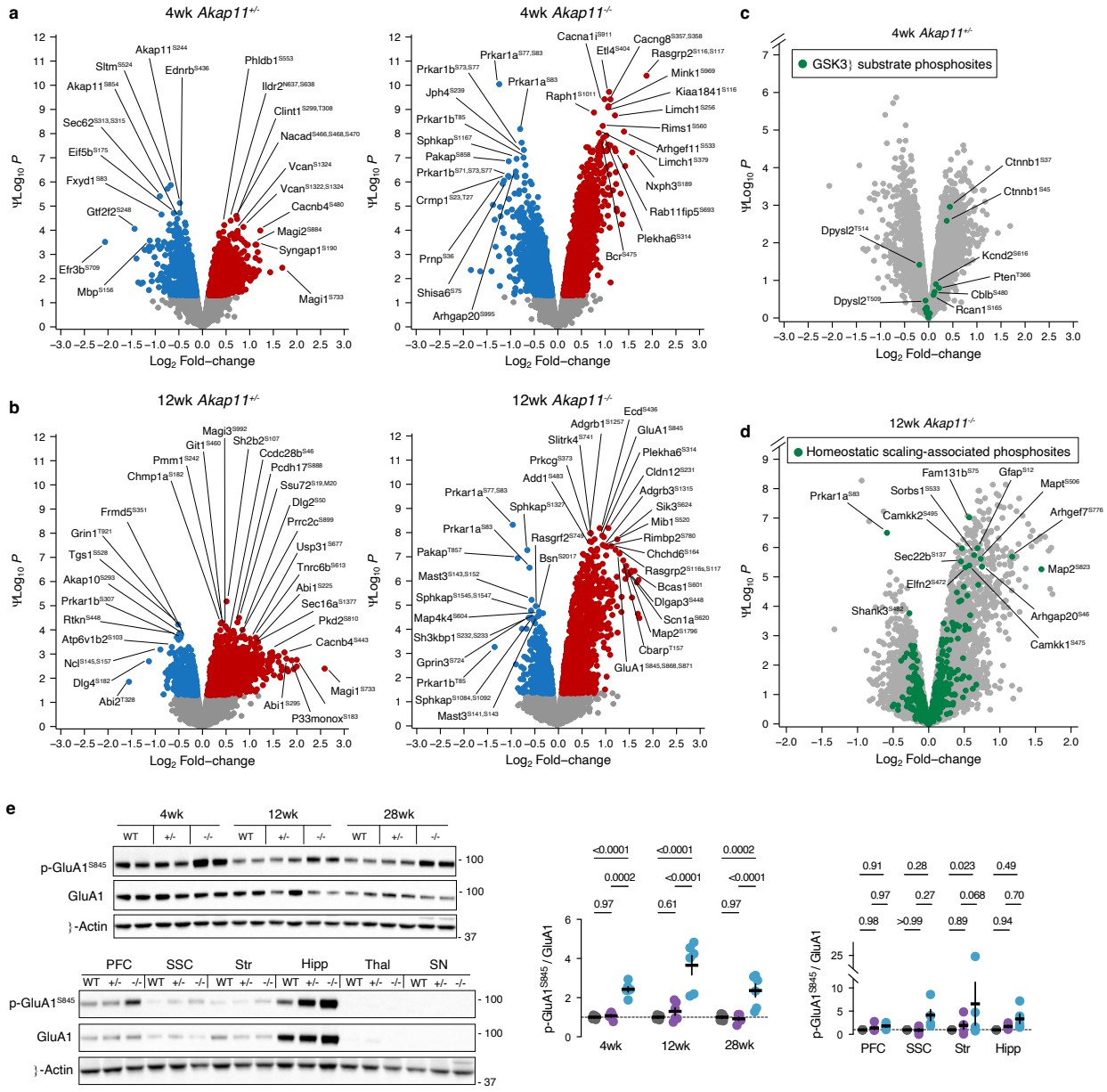

Extended Data Fig. 4: Phosphoproteomic correlates of synaptic plasticity, related to Fig. 4.

a, Volcano plots of synapse phosphoproteomics in 4wk *Akap11* mutants relative to WT. Upregulated and downregulated DAPPs are colored red and blue respectively. AKAP11 phosphopeptides are omitted from *Akap11*$^{-/-}$ plots, for clarity.

b, Volcano plots of synapse phosphoproteomics in 12wk *Akap11* mutants relative to WT. Upregulated and downregulated DAPPs are colored red and blue respectively. AKAP11 phosphopeptides are omitted from *Akap11*$^{-/-}$ plots, for clarity.

c, Volcano plots of 4wk synapse phosphoproteomics for *Akap11*$^{+/-}$. Known GSK3β substrates from PhosphoSitePlus are labeled in green.

d, Volcano plots of 12wk synapse phosphoproteomics for *Akap11*$^{+/-}$. Phosphosites that are altered during scaling (24 hours of bicuculline or tetrodotoxin treatment, FDR <0.05 in Desch et al., 2021)[60] are labeled in green.

e, Immunoblotting and quantification of p-GluA1^{S845} and GluA1 in 4wk, 12wk or 28wk cortical lysate or in microdissected brain regions. Two-way ANOVA with Tukey's post hoc test. See Supplementary Table 1 for statistics.

Extended Data Figure 5

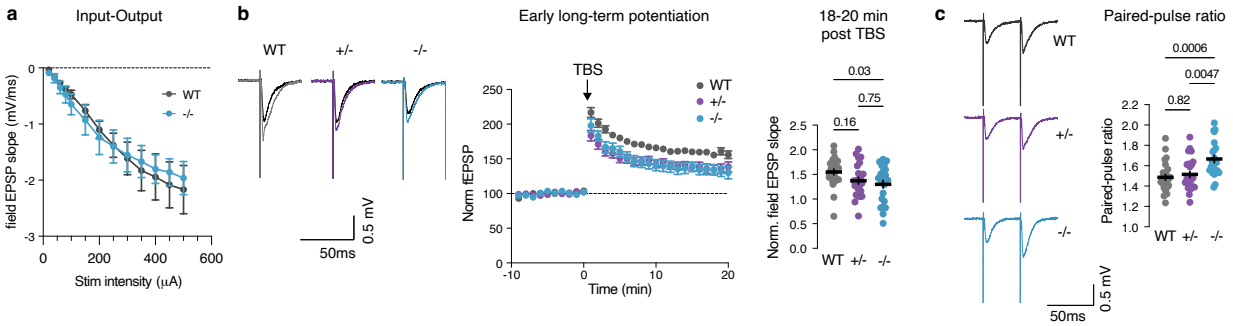

Extended Data Fig. 5: Electrophysiological characterization of synaptic strength and plasticity, related to Fig. 4.
a, Input-output (I-V) curves of field electric postsynaptic potential (EPSP) responses evoked with varying stimulation intensities (20-500uA).
b, Left, representative traces of field EPSPs before and after LTP induced by theta burst stimulation (TBS). Traces were generated by averaging the data points during the first (baseline; light lines) and last (post LTP; dark lines) two mins of the experiment. Middle, quantification of field EPSP slopes over the 30-min long early LTP experiment. Each dot represents the average field EPSP slope over 1 min. Right, quantification of field EPSP slope in minutes 18-20 following TBS.
c, Left, representative traces of paired pulse responses at 40ms stimulation intervals. Right, quantification of paired pulse ratios from *Akap11* mutants and WT brain slices.
a-c, Data are represented as mean +/- SEM. One-way ANOVA with Tukey's post hoc test. See Supplementary Table 1 for statistics.

Extended Data Figure 6

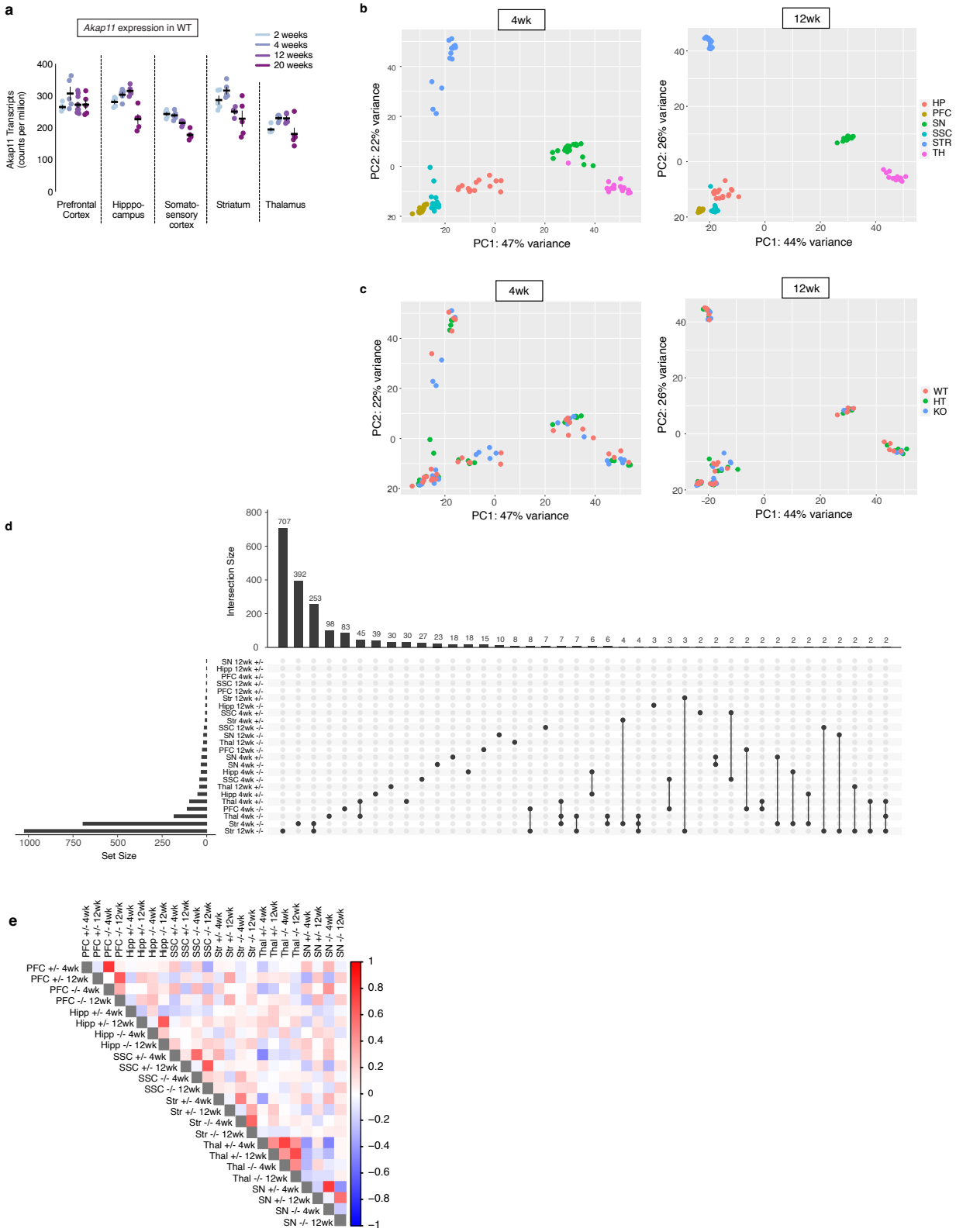

Extended Data Fig. 6: Comparisons between brain regions, ages, and genotypes in bulk RNA sequencing, related to Fig. 5.

a, *Akap11* mRNA expression across brain regions and ages in wild-type mice, analyzed from data published in Farsi et al., 2023[11]. Data are represented as mean +/- SEM.
b, PCA plots of bulk RNA sequencing experiments, colored by brain region.
c, PCA plots of bulk RNA sequencing experiments, colored by genotype.
d, Upset plot showing overlapping and unique DEGs (FDR < 0.05) across brain regions, ages and genotypes in bulk RNA sequencing experiments.
e, Log_2FC correlations between nominally significant genes ($P < 0.05$) across brain regions, ages, and genotypes. Color indicates Spearman correlation values.

Extended Data Figure 7

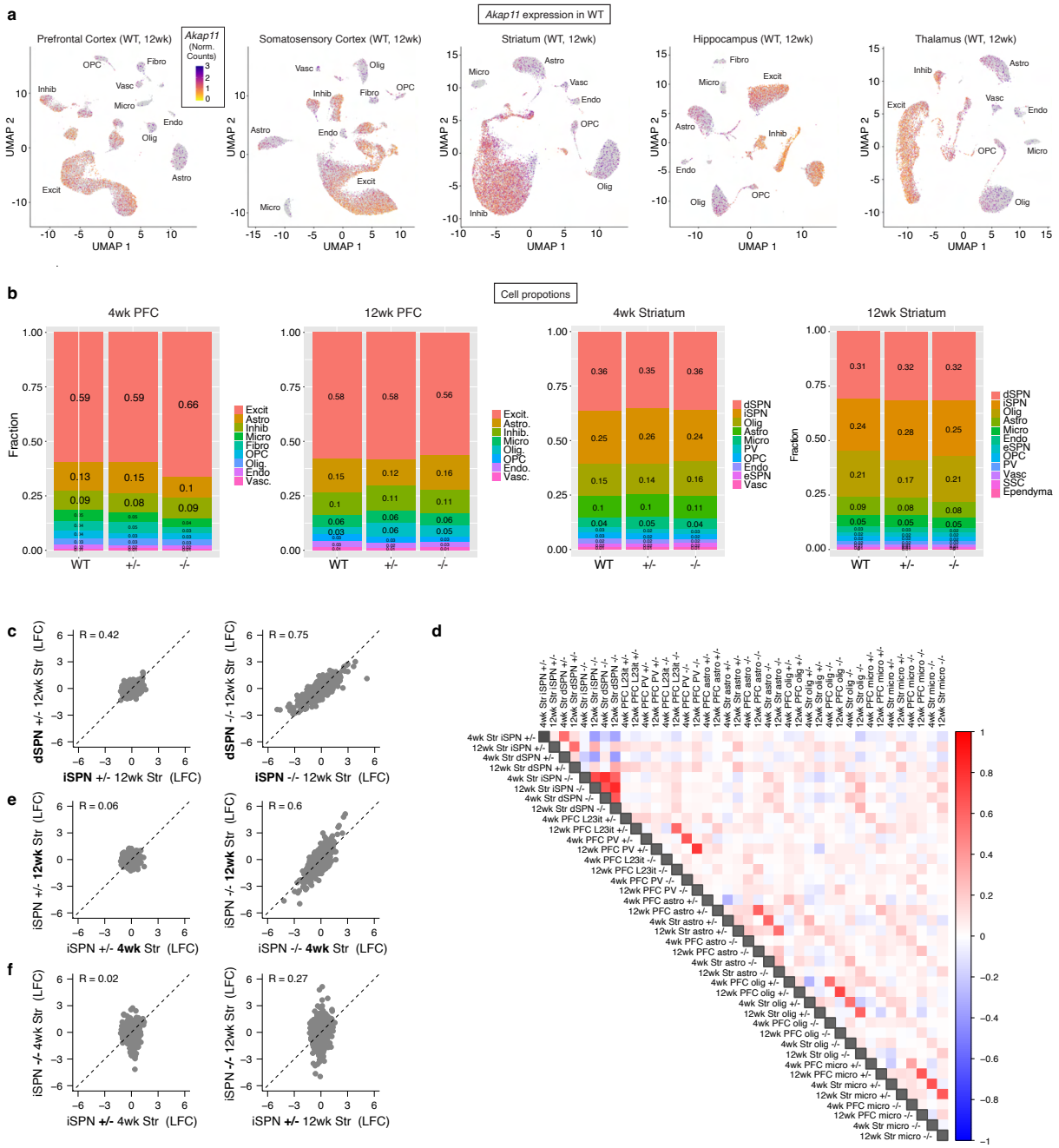

Extended Data Fig. 7: Comparisons between brain regions, age and cell types in snRNA-seq, related to Fig. 5. **a,** *Akap11* expression across major cell types on uniform manifold approximation and projection (UMAP) representations of cell types in different brain regions and ages of wild-type mice. This data appears in Farsi et al., 2023[11]. **b,** Fraction of each cell type identified across genotypes. **c,** Log_2FC scatterplots comparing all genes for iSPN vs dSPN subtypes. **d,** Log_2FC correlations between nominally significant genes ($P < 0.05$) across cell types. Color indicates Pearson correlation values. **e,** Log_2FC scatterplots comparing all genes at 4wk vs. 12wk, in iSPNs. **f,** Log_2FC scatterplots comparing all genes in *Akap11*$^{+/-}$ vs. *Akap11*$^{-/-}$, in iSPNs.

Extended Data Figure 8

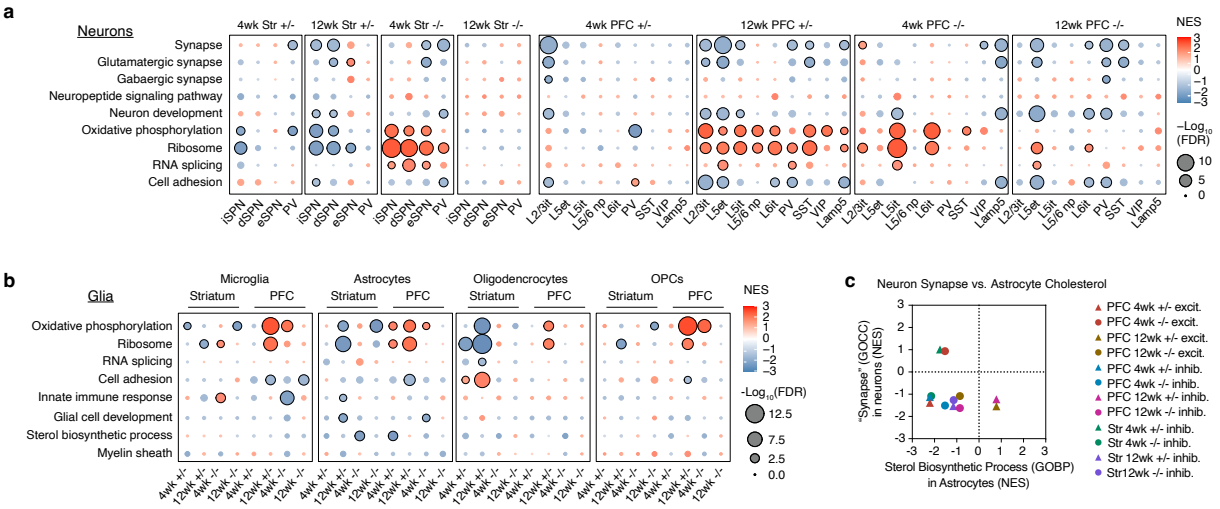

Extended Data Fig. 8: Neuronal-synapse and astrocyte-cholesterol related transcriptomic changes detected by snRNA-seq, related to Fig. 5..

a, GSEA from neurons identified by snRNA-seq of striatum and PFC, showing MsigDB pathways of interest.

b, GSEA results from glia snRNA-Seq, showing, showing MsigDB pathways of interest, including pathways related to glia function.

c, Comparison of NES from synapse pathways in neurons vs. cholesterol biosynthesis pathways in astrocytes.

Extended Data Figure 9

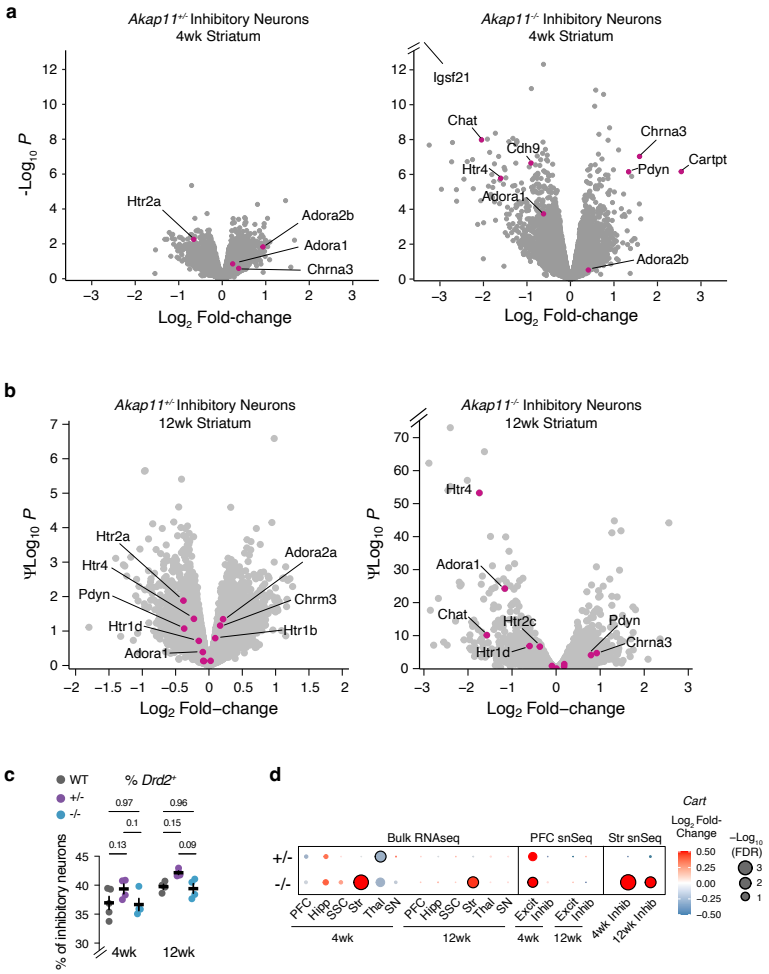

Extended Data Fig. 9: Evidence for transcriptomic alteration of neuromodulation-related genes, related to Fig. 5.
a, Volcano plots of transcriptomic changes identified by snRNA-seq analysis in 4wk striatal inhibitory neurons. Genes of interest related to neuromodulation and circuit development are highlighted in magenta.
b, Volcano plots of transcriptomic changes identified by snRNA-seq analysis in 12wk striatal inhibitory neurons. Genes of interest related to neuromodulation and circuit development are highlighted in magenta.
c, Percentage of Drd2^{+} inhibitory neurons in the striatum. Data are represented as mean +/- SEM. Two-way ANOVA with Tukey's post hoc test.
d, Log_2FC and FDR-adjusted *P*-values for *Cart* across bulk and snRNA-seq.

Extended Data Figure 10

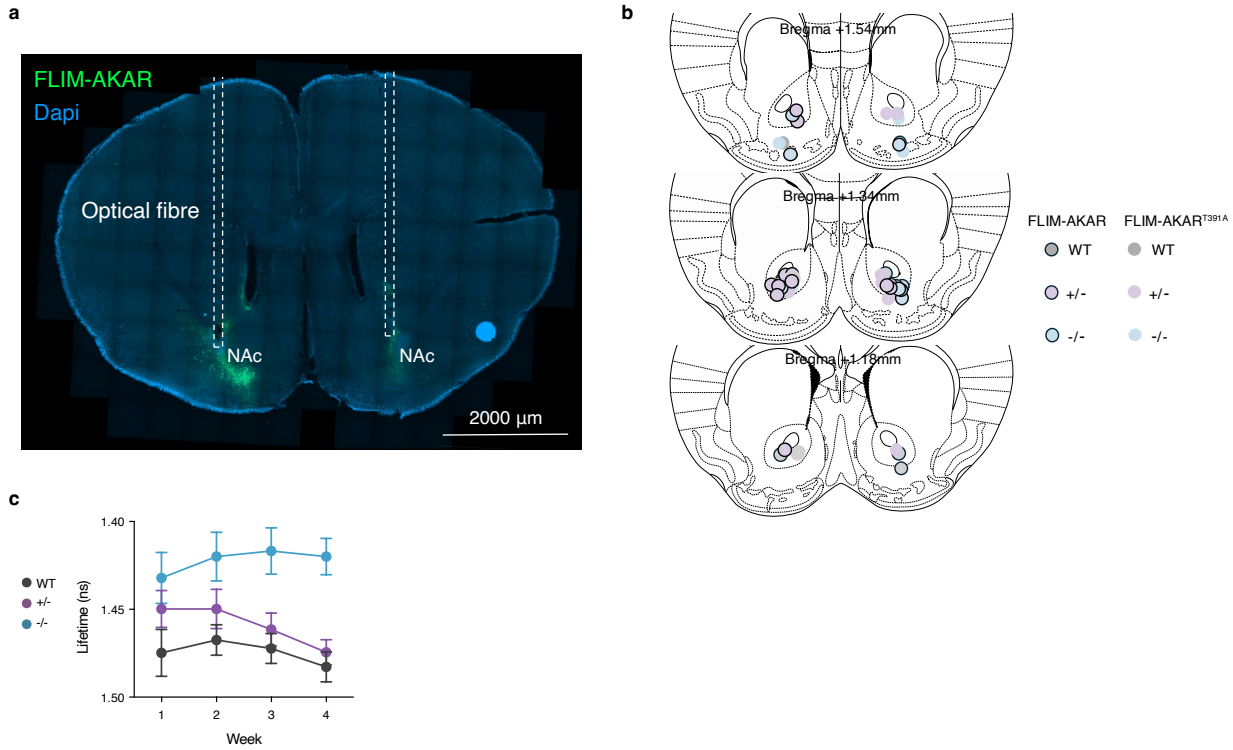

Extended Data Fig. 10: FLIM-AKAR injections sites and longitudinal measurement of PKA activity, related to Fig. 6. **a,** Immunohistochemical validation of AAV injection site targeting of NAc. **b,** Injection site targets of each animal in this study. Animals of different genotypes are differentiated by color, and FLIM-AKAR variants that were injected into contralateral hemispheres are differentiated by black border. **c,** Fluorescence lifetime of FLIM-AKAR across 4 fiber photometry recording sessions across weeks.

Supplementary Table 1: Statistical information.

Supplementary Table 2: Results of synapse proteomics and phosphoproteomics of *Akap11* mutant mice.

Supplementary Table 3: Significant pathways identified by gene set enrichment analysis of synapse proteomes of *Akap11* mutant mice.

Supplementary Table 4: Nominally significant genes from bulk RNA sequencing of *Akap11* mutant mice.

Supplementary Table 5: Significant pathways identified by gene set enrichment analysis of bulk RNA sequencing of *Akap11* mutant mice.

Supplementary Table 6: Nominally significant genes from single nucleus RNA sequencing of *Akap11* mutant mice.

Supplementary Table 7: Significant pathways from gene set enrichment analysis of bulk RNA sequencing of *Akap11* mutant mice.

Acknowledgements

We thank Kris Dickson and members of the Sheng and Granger Labs for valuable input; Ben Neale, Tarjinder Singh and Calwing Liao for consultations on human genetic evidence; Kira Brenner and Jacalyn Fahey for assistance with immunohistochemistry; Miriam Kpoyto for help with amphetamine-induced hyperlocomotion experiments; Michael Dolan and Chuck Vanderburg for guidance on transcriptome experiments; Michael Sherman for packaging AAVs; Deeksha Misri for bulk RNAseq analysis advice; Tyler Caron and Matthew Beck for help with mouse colony management and *in vivo* experiment logistics; the Broad Institute Genomic Platform for assistance with RNA sequencing.

Author contributions

B.J.S. and M.S. conceived and designed the -omics, biochemical, and behavioral experiments**.** Y.G., M.S. and A.G. conceived and designed fiber photometry, electrophysiology, pharmacological and behavioral experiments. B.J.S. and M.S. wrote the manuscript, with help from Y.G and A.G. and input from all authors. B.J.S. and Y.G. performed the majority of experiments and analyses in this paper. Specifically, B.J.S. performed immunoprecipitations, immunoblots, immunohistochemistry, synapse purifications, nuclei isolation, RNAseq, homecage activity measurements and analyzed these data. Y.G. performed FLiP measurements, slice electrophysiology, dopamine receptor pharmacology, amphetamine-induced hyperlocomotion and analyzed these data. A.N. processed the transcriptome data, including quality control, reference genome alignment, cell type clustering, annotation and differential expression analysis, with guidance from S.K.S., K.P.M. and supervision from J.L. M.J.K. performed nuclei isolation and library preparation for 12 week striatum and PFC snSeq datasets. B.L. designed the FLiP recording set up, calibrated the measurements and developed the analysis pipeline with guidance from B.L.S. K.B. performed LC-MS/MS for synapse proteomics and synapse phosphoproteomics and A.V.T. performed LC-MS/MS for immunoprecipitations with guidance from H.K. and S.C and analysis help from D.R.M. J.A. and C.G. helped with immunoblots. S.N. performed smFISH. I.P. and N.S. assisted with brain tissue collection and immunohistochemistry. H.P. and N.M.N. assisted with nuclei isolation and snSeq library preparation with supervision from E.Z.M. E.Z.M. designed the snSeq protocol and guided snSeq analysis. S.A., Z.F. and X.L. helped with data analysis. N.M. conducted phosphoproteomics motif analysis with supervision from B.S. B.D. purified synapse fractions for proteomics/phosphoproteomics and provided guidance and supervision for biochemical experiments. M.S. and A.G. supervised the project and acquired funding. This work was supported by the Stanley Center for Psychiatric Research and the Harvard Brain Science Initiative Bipolar Disorder Seed Grant.

Declaration of Interests

M.S. is cofounder and scientific advisory board (SAB) member of Neumora Therapeutics and serves on the SAB of Biogen, Proximity Therapeutics and Illimis Therapeutics. S.A.C. is a member of the SAB of Kymera, PTM BioLabs, Seer, and PrognomIQ. B.S. serves on the Scientific Advisory Board of Annexon Biosciences and is a minor shareholder of Annexon. B.D. is a full-time employee of Vigil Neuroscience. E.Z.M. is an academic founder of Curio

975 Bioscience.
976
977 **Methods**
978
979 Animals
980 All experiments were approved by the Broad Institute IACUC (Institutional Animal Care and Use
981 Committee) and conducted in accordance with the NIH Guide for the Care and Use of
982 Laboratory Animals. Heterozygous *Akap11* mice (B6.Cg-Akap11[tm1.2Jsco/J]) were obtained
983 from The Jackson Laboratory following cryorecovery (strain #028922). As previously
984 described[23], these mice have deletions of exons 6 and 7 of the mouse *Akap11* gene to create a
985 knockout allele. *Akap11* mutant mice were deposited by the donor lab after 6 generations of
986 backcrossing to the C57BL/6J background. We confirmed the genetic background of the
987 animals to be greater than 90% C57BL/6J through SNP analysis (MiniMuga panel, Transnetyx).
988 To establish the colony, founders were crossed to WT C57/BL6J mice (Jackson Laboratory,
989 #000664) for one generation. Subsequently, heterozygous mice were crossed with each other
990 to produce wild-type (WT, +/+), heterozygous (Het, +/-) and knockout (KO, -/-) littermates used
991 for experiments. Mice were housed at AAALAC-approved facilities on a 12-hour light/dark cycle,
992 with food and water available ad libitum. For fluorescence lifetime photometry experiments
993 (FLiP), mice were housed in a 12h/12h light/dark reverse cycle. FLiP and pharmacological
994 experiments were conducted in compliance with protocols approved by the Harvard Standing
995 Committee on Animal Care, adhering to guidelines outlined in the US National Institutes of
996 Health Guide for the Care and Use of Laboratory Animals.
997
998 Anti-AKAP11 antibodies
999 Two custom polyclonal rabbit anti-AKAP11 antibodies were generated for this paper and used
1000 for immunoblot experiments. For both polyclonal antibodies, the first 284 amino acids of the
1001 mouse AKAP11 protein (Uniprot reference E9Q777) were injected into rabbits, and affinity
1002 purified by a company (Genscript). The antigen sequence used was:
1003 MAAFQPLRSSHLKSKASVRKSFSEDVFRSVKSLLQSEKELCSVSGGECLNQDEHPQLTEVTFL
1004 GFNEETDAAHIQDLAAVSLELPDLLNSLHFCSLSENEIICMKDTSKSSNVSSSPLNQSHHSGML
1005 CVMRVSPTLPGLRIDFIFSLLSKYAAGIRHTLDMHAHPQHHLETTDEDDDDTNQSVSSIEDDFVT
1006 AFEQLEEEENAKLYNDEINIATLRSRCDAASQTTSGHHLESHDLKVLVSYGSPKSLAKPSPSVN
1007 VLGRKEAASVKTSVTTSVSEPWTQRSLY and were validated by immunoblot comparisons
1008 between WT and *Akap11*$^{-/-}$ brain tissue. For immunoprecipitations, we used a commercial rabbit
1009 monoclonal antibody targeting residues surrounding Alanine 1125 of mouse AKAP11 (Cell
1010 Signaling Technologies (CST), #77313). All other AKAP11 antibodies we tested, including our
1011 own polyclonal antibodies, immunoprecipitated PKA subunits in *Akap11*$^{-/-}$ brains, indicating
1012 insufficient specificity (data not shown but available upon request).
1013
1014 Immunoprecipitation
1015 Twelve week-old (P120) male mice were euthanized using CO_2 inhalation, harvested around the
1016 lights-off period (Zeitgeber Time 12, ZT12) when mice are active, which was approximately
1017 ZT10-ZT14. For coIP-MS, 5 WT, 5, *Akap11*$^{+/-}$, and 5 *Akap11*$^{-/-}$ animals underwent
1018 immunoprecipitation with the AKAP11 antibody. Three WT animals underwent

1019 immunoprecipitation with IgG control. After sacrifice, cortical hemispheres were rapidly
1020 dissected and mechanically homogenized with 12 slow strokes by a Teflon homogenizer and a
1021 glass vessel in ice-cold phosphate buffered saline (PBS) with 1% Triton-X with protease (Sigma
1022 4693159001) and phosphatase (Sigma 4906837001) inhibitors. The homogenate was
1023 centrifuged at 10,000 g (4°C) for 10 minutes and the resultant supernatant was used for
1024 immunoprecipitation. Protein concentration was measured with bicinchoninic acid assay BCA
1025 (Thermo Fisher Scientific A53225) and samples were normalized to equal protein
1026 concentrations and volumes with homogenization buffer in protein LoBind tubes (Eppendorf
1027 #022431102). For coIP-mass spectrometry, samples had 4mg of protein in a volume of 2mL.
1028 For coIP-immunoblot, samples had either 500µg or 1mg (which were matched between
1029 experimental and control samples), normalized to 1 mg/mL. Lysates were incubated overnight
1030 rotating at 4°C with 1µg anti-AKAP11 monoclonal antibody (1:20; CST 77313) or 1µg mAb IgG
1031 control (CST 3900) for mass spectrometry experiments. For coIP-immunoblot, lysates were
1032 incubated with the following primary antibodies: 1:50 Rabbit anti-AKAP11 (CST 77313), 1:50
1033 Rabbit anti-GluA1 (CST 13185), 1:50 Rabbit anti-PKA Cα (CST 4782), 1:50 Rabbit anti-PKA
1034 R1α (CST 5675), 1:50 Rabbit anti-PKA R2β (Sigma ABS14), 1:50 Rabbit anti-VAPA
1035 (Proteintech 15275-1-AP), 1:50 Rabbit anti-VAPB (Proteintech 14477-1-AP), 1:50 Rabbit anti-
1036 GSK3α (CST 4337), 1:50 Rabbit anti-GSK3β (CST 12456), 1:50 Mouse anti-DYRK1A (Abnova
1037 H00001859-M01), 1:50 Mouse anti-P62 (Abcam ab56416). As additional negative controls,
1038 Rabbit mAb IgG (CST 3900), Normal Rabbit IgG (CST 2729) or Mouse mAb IgG2a Isotype
1039 Control (CST 61656) were diluted according to manufacturer's instructions and added in lieu of
1040 primary antibodies.
1041
1042 The next day, lysate-antibody mixtures were incubated with Dynabead Protein G (Invitrogen
1043 1004D) for 1 hour at room temperature (RT), following the manufacturer's specifications. Beads
1044 were then washed three times for 10 min with PBS containing 0.02% Tween20. For coIP-
1045 immunoblotting, proteins were eluted from magnetic beads with 1x Laemmli buffer and beta-
1046 mercaptoethanol (BME) mixture (Boston biosciences BP111R, Biorad 1610737, Sigma) and
1047 boiled at 98°C for 8 min and subsequently examined by SDS-PAGE (immunoblot). For coIP-MS,
1048 samples were washed twice with ice cold 50mM Tris-HCl pH 7.5 and transferred to a new tube.
1049 Subsequently samples were resuspended in 50µl ice cold Tris-HCl pH 7.5.
1050
1051 <u>CoIP sample preparation for Liquid Chromatography-Mass Spectrometry/Mass Spectrometry</u>
1052 <u>(LC-MS/MS) analysis</u>
1053 Samples were incubated in 80 µl of urea-based digestion buffer (30 mM Tris-HCl pH=8, 0.4 µg
1054 trypsin, 1mM dithiothreitol, 2 M Urea) at 25℃ and 1000 rpm for 1h. The supernatant was then
1055 collected, followed by a second incubation in 80 µl of the same urea-based buffer at 25℃ and
1056 1000 rpm for 30 min. The second supernatant was also collected. The beads were washed with
1057 60 µL of wash buffer (2M Urea, 50mM Tris-HCl pH=8 wash buffer) two times, collecting both
1058 washes. The on-bead digests (supernatants) and two washes were combined into 280 µl per
1059 sample and reduced with 2.3 µl of 500mM dithiothreitol (DTT) for 30 min at 1000 rpm at 25℃.
1060 This was followed by alkylation with 4.6 µl of 500 mM iodoacetamide (IAA) for 45 min at 1000
1061 rpm at 25℃. The samples were digested overnight with 0.5 µg of Trypsin at 700 rpm at 25℃.
1062 Reactions were quenched with formic acid (FA) at a final concentration of 1%, then desalted

1063 using reverse-phase C-18 StageTips as previously described[39] and dried down. The peptides
1064 were reconstituted in 80 µl 50mM HEPES, followed by 8 µl of neat acetonitrile (MeCN), and
1065 isobarically labeled using 500 µg of Tandem Mass Tag 18-plex (TMT18) reagent (Thermo
1066 Fisher Scientific A44520 & A52046) for 1h at 1000 rpm and 25℃. After confirming successful
1067 labeling (> 95% label incorporation), the reactions were quenched with 4 µl of 5%
1068 hydroxylamine. Samples were mixed and dried. The sample was resuspended in 300 µl of 0.1%
1069 formic acid to proceed with fractionation by bRP fractionation strategy on StageTips. The tips
1070 were packed with 3 plugs of Empore Extraction Disks SDB-RPS 47mm material. StageTips
1071 were sequentially conditioned with 100 µl of methanol (MeOH) and 100 µl of
1072 50%MeCN/0.1%FA. The sample was loaded onto the StageTips, and washed twice with 100 µl
1073 of 0.1% FA. 25 µl of 20 mM ammonium formate was added to the stage tip for buffer exchange.
1074 It was then eluted into 8 consecutive fractions with increased organic content at 100 µl per
1075 elution step (5, 10, 15, 20, 23, 27, 30 and 45% MeCN in 20 mM ammonium formate). The
1076 fractions were transferred to HPLC vials and dried.
1077
1078 LC-MS/MS analysis of coIP samples
1079 The samples were analyzed on a Q Exactive HF-X mass spectrometer with a Vanquish Neo
1080 UHPLC system (Thermo Fisher Scientific). The solvents used for the HPLC system were
1081 solvent A (0.1% FA) and solvent B (0.1% FA/100% MeCN). The samples were injected into a
1082 75-µm ID PicoFrit column packed manually to approximately 28 cm of length with ReproSil-Pur
1083 C18-AQ 1.9-µn beads (Dr. Maisch) and heated to 50℃ for chromatographic separation.
1084 The bRP fractions were loaded into the column at a flow rate of 200nL/min. The
1085 chromatography consists of a 110-min method with a gradient of 1.6–5.4% solvent B for 1 min,
1086 18–27% B for 22 min, 27–54% B for 9 min, 54–72% B for 1 min, followed by a hold at 72% B for
1087 5 min and 72%-45% B for 10 min. The mass spectrometer was operated in data-dependent
1088 acquisition mode. The MS parameters were set as follows: MS1, r=60,000; MS2, r=15,000; MS1
1089 AGC target of 3e6 with maximum injection time of 10ms; MS2 for the 20 most abundant ions
1090 using an AGC target of 5e4 and maximum injection time of 105ms; and normalized collision
1091 energy of 28.
1092 Data analysis of the coIP-LC-MS/MS experiment
1093 Collected data were analyzed using the Spectrum Mill software package (Broad Institute). All
1094 extracted spectra were searched against a UniProt database containing mouse reference
1095 proteome sequences retrieved on 04/07/2021 and containing 55734 entrees. Fixed
1096 modifications were carbamidomethylation at cysteine. TMT labeling was required at lysine, but
1097 peptide N termini could be labeled or unlabeled. Allowed variable modifications were protein N-
1098 terminal acetylation and oxidized methionine.
1099
1100 Protein quantification was achieved by taking the ratio of TMT reporter ions for each sample
1101 over the median of all channels. TMT18 reporter ion intensities were corrected for isotopic
1102 impurities in the Spectrum Mill protein/peptide summary module using the afRICA correction
1103 method which implements determinant calculations according to Cramer's Rule79 and
1104 correction factors obtained from the reagent manufacturer's certificate of analysis for lot
1105 numbers XD343709 and XD346675. After performing median-MAD normalization, a moderated
1106 two-sample t-test was applied to the datasets to compare WT, *Akap11*$^{+/-}$ and *Akap11*$^{-/-}$ sample

1107 groups.
1108
1109 Immunoblot
1110 Four week (P30) or 12 week (P120) male mice were euthanized using CO_2 inhalation between
1111 ZT10-ZT14, after which whole cortices were rapidly dissected and flash-frozen in liquid nitrogen.
1112 Single hemispheres were homogenized in a 5 ml ice-cold homogenization buffer (1% SDS in
1113 PBS) supplemented with phosphatase (Sigma 4906837001) and protease inhibitors (Sigma
1114 4693159001), using the mechanical homogenization procedure described above. After BCA
1115 (Thermo Fisher Scientific, A53225 or 23225) quantification of protein concentration, samples
1116 were diluted with 6X Laemmli buffer with BME (Boston Bioproducts, BP-111R) or 2x Laemmli
1117 buffer (Biorad, 1610737) with BME (Sigma, M3148) to a final concentration of 1x and boiled in
1118 reducing SDS loading buffer at 98°C for 8 min. After preparation, sample aliquots were frozen at
1119 -80°C. Before running on a gel, samples were thawed, heated at 98°C for 1 min and centrifuged
1120 briefly. Samples were run on NuPAGE 3-8% Tris Acetate gradient gels (Invitrogen) at a
1121 constant voltage. Equal amounts of sample were loaded unless otherwise specified (Extended
1122 Data Figs. 3a,b). For Fig. 2a, a subset of smaller molecular weight proteins were tested on 4-
1123 20% tris glycine gradient gels (Invitrogen). Proteins were transferred to 0.2 mm nitrocellulose
1124 membranes using semi-dry transfer (Bio-Rad Transblot Turbo; 25V 30 min) and visualized by
1125 Coomassie stain (Sigma, P7170). Subsequently, membranes were blocked with 5% milk in Tris-
1126 buffered saline with 0.2% Tween 20 (TBST). Membranes were incubated overnight with primary
1127 antibodies in 5% milk TBST with gentle rotation at 4°C. Membranes were incubated with primary
1128 antibodies overnight at 4°C, washed three times with TBST for 10 min, and then incubated with
1129 secondary HRP-conjugated antibodies raised against the appropriate species for 1 hour at RT.
1130 After 3 additional TBST washes, membranes were imaged on ChemiDoc MP (Bio-Rad) and
1131 analyzed using Image Lab Software (Bio-Rad). Enhanced chemiluminescence (Thermo, 34580
1132 and 34096) and exposures were optimized to obtain signals in the linear range. Membranes
1133 were then stripped (Thermo, 46430),washed three times, re-blocked with 5% milk in TBST, and
1134 re-probed as described above. For cortical lysate immunoblots, 20µg of protein was loaded. For
1135 microdissected brain regions, 15 or 20 µg or protein and 5 or 10 µg synapse fraction protein
1136 were used for SDS-PAGE, unless otherwise specified (Extended Data Fig. 3a,b). For all
1137 experiments, protein loading amounts were consistent across samples.
1138
1139 For coIP-immunoblot, the following antibodies were used during SDS-page (after
1140 immunoprecipitation): 1:1000 Mouse anti-PKA R1α (BD 610609), 1:1000 Mouse anti-PKA Cα
1141 (BD 610980), 1:1000 Mouse anti-PKA R2β (BD 610625), 1:1000 Mouse anti-GluA1 (NeuroMab
1142 75-327), 1:1000 Rabbit anti-Vinculin (CST 4650), 1:1000 Rabbit anti-VAPA (Proteintech 15275-
1143 1-AP), 1:1000 Rabbit anti-VAPB (Proteintech 14477-1-AP), 1:1000 Rabbit anti-GSK3α (CST
1144 4337), 1:1000 Rabbit anti-GSK3β (CST 9315), Mouse anti-GSK3α/β (Thermo Fisher Scientific
1145 44-610) ,1:1000 Rabbit anti-Dyrk1a (CST 2771), 1:1000 Rabbit anti-P62 (CST 5114). For coIP-
1146 immunoblot, we used horseradish peroxidase (HRP)-conjugated secondaries recognizing the
1147 host species of the primary antibody (Thermo Fisher Scientific 31460 and 31430 for rabbit and
1148 mouse respectively). When the IP and immunoblot antibodies were from the same species (Fig.
1149 1g), we used secondaries that are selective towards non-denatured IgG (1:1000, TrueBlot HRP,
1150 Rockland, 18-8816-33 and 18-8817-30).

1151
1152 For immunoblot, the following antibodies were used:
1153 1:1000 Rabbit anti-AKAP11 (Custom R171), 1:1000 Rabbit anti-AKAP11 (Custom R173),
1154 1:1000 Mouse anti-PKA R1α (Thermo Fisher Scientific MA5-24981), 1:1000 Rabbit anti-PKA
1155 R1α (CST 5675), 1:1000 Rabbit anti-PKA Cα (CST 4782), 1:1000 Rabbit anti-Iqgap1 (Abcam
1156 ab86064), 1:1000 Rabbit anti-Dyrk1a (CST 2771), 1:1000 Rabbit anti-GSK3α (CST 4818),
1157 1:1000 Rabbit anti-GSK3β (CST 9315), 1:1000 Mouse anti-P62 (Abcam ab56416), 1:1000
1158 Rabbit anti-LC3A/B (CST 12741), 1:1000 Rabbit anti-VAPA (Proteintech 15275-1-AP), 1:1000
1159 Rabbit anti-β Catenin (CST 8480), 1:1000 Mouse anti-Protein Phosphatase 1 (Santa Cruz SC-
1160 7482), 1:1000 Rabbit anti-Sik2 (CST 6919), 1:1000 Rabbit anti-p-GSK3α^{S21} / anti-p-GSK3β^{S9}
1161 (CST 8566), 1:1000 Rabbit anti-p-GSK3α / anti-p-GSK3β (CST 5676), 1:1000 Rabbit anti- p-
1162 GSK3β^{S9} (CST 9336), 1:1000 Rabbit anti- p-GluA1^{S845} (CST 8084), 1:1000 Rabbit anti- GluA1
1163 (CST 13185), 1:1000 Mouse anti- GluA1 (NeuroMab 75-327), 1:1000 Mouse anti-PSD95
1164 (BioLegend 810301), 1:1000 Rabbit anti-Homer1 (Synaptic Systems 160003), 1:1000 Guinea
1165 Pig anti-Synaptophysin 1(Synaptic Systems 101004). 1:1000 Mouse anti-PSD95 (clone K28/43,
1166 Antibodies Inc 75-028). HRP-conjugated anti-Rabbit or anti-Mouse IgG (Thermo Fisher
1167 Scientific 31460 and 31430). β-actin was probed using an HRP conjugated primary antibody
1168 after all other proteins were probed (1:10,000. Thermo Fisher Scientific A3854). Otherwise, we
1169 used HRP conjugated secondaries recognizing the host species of the primary antibody
1170 (Thermo Fisher Scientific 31460 and 31430 for rabbit and mouse respectively).
1171
1172 Synapse purifications
1173 Synapse fractions were purified as we described previously[39,99,100]. Flash-frozen whole cortex
1174 and subcortical basal forebrain was mechanically homogenized with 12 slow strokes by a Teflon
1175 homogenizer and glass vessel in ice-cold homogenization buffer (5 mM HEPES pH 7.4, 1 mM
1176 $MgCl_2$, 0.5 mM $CaCl_2$, supplemented with phosphatase (Sigma 4906837001) and protease
1177 inhibitors (Sigma 4693159001). The homogenate was centrifuged for 10 min at 1,400 g (4°C)
1178 and the resulting supernatant (S1) was re-centrifuged at 13,800 g for 10 min (4°C). The
1179 resulting pellet (P2) was resuspended in 0.32 M Sucrose, 6 mM Tris-HCl (pH 7.5) and layered
1180 gently on a 0.85 M, 1 M, 1.2 M discontinuous sucrose gradient (all layers in 6 mM Tris-HCl pH
1181 7.5) and ultracentrifuged at 82,500 g for 2 hours (4°C). For synapse mass spectrometry
1182 experiments, phosphatase inhibitors were added to 1 M and 1.2 M sucrose buffers. The
1183 synaptosome fraction, which sediments at the interface between 1 M and 1.2 M sucrose, was
1184 collected. An equal volume of ice-cold 1% Triton X-100 (in 6 mM Tris-HCl pH 7.5) was added,
1185 mixed thoroughly, and incubated on ice for 15 min. The mixture was ultracentrifuged at 32,800 g
1186 for 20 min (4°C), and the pellet (the synapse fraction) was collected by resuspension in 1%
1187 SDS. A small aliquot was taken to measure the protein concentration using the Pierce Micro
1188 BCA assay (ThermoFisher Scientific, 23235) or BCA (ThermoFisher Scientific A53225) and the
1189 remaining protein was stored at -80°C until processed for MS or immunoblot. For synapse
1190 proteomics, sixteen synaptic fractions extracted from the cortex of wild type, *Akap11*$^{+/-}$ and
1191 *Akap11*$^{-/-}$ mouse brains were used for the proteomics study using tandem mass tag (TMT)
1192 isobaric labeling strategy for quantitation. At 4 weeks, sample sizes were n= 5 WT, 5 *Akap11*$^{+/-}$
1193 and 6 *Akap11*$^{-/-}$. At 12 weeks, the sample sizes were n= 6 WT, 5 *Akap11*$^{+/-}$ and 5 *Akap11*$^{-/-}$.
1194

1195 Processing of samples for proteomics and phosphoproteomics
1196 Synapse fractions from animals at 4 weeks and 12 weeks were processed in two separate
1197 TMT16 plexes as described before[39]. Briefly, all samples were prepared in a 1% SDS buffer and
1198 digested using S-Trap™ sample processing technology (Protifi) following manufacturers
1199 recommendations. Following digestion, 100 µg of each sample was reconstituted in 20µl of
1200 50mM HEPES and labeled with 200 µg TMT16 reagent (Thermo Fisher Scientific A44520). After
1201 verifying successful labeling of more than 95% label incorporation reactions were quenched,
1202 mixed, desalted and dried down. TMT16 labeled peptides were fractionated by high pH
1203 reversed-phase chromatography on a 4.6 mm x 250 mm Zorbax 300 extend-c18 column
1204 (Agilent). One-min fractions were collected during the entire elution and fractions were
1205 concatenated into 18 proteome fractions for LC-MS/MS analysis. Five percent of each fraction
1206 was removed for proteome analysis. The remaining of each of the 18 fractions were further
1207 concatenated to 9 fractions and dried down for phosphopeptide enrichment using immobilized
1208 metal affinity chromatography (IMAC).
1209
1210 LC-MS/MS analysis for synapse fractions
1211 One microgram of each proteome fraction and half of each of the IMAC fractions were analyzed
1212 on a QE-HFX mass spectrometer (Thermo Fisher Scientific) coupled to an Easy-nLC 1200 LC
1213 system (Thermo Fisher Scientific). Samples were separated using 0.1% Formic acid/3%
1214 Acetonitrile as buffer A and 0.1% Formic acid /90% Acetonitrile as buffer B on a 27cm 75um ID
1215 picofrit column packed in-house with Reprosil C18-AQ 1.9 mm beads (Dr Maisch GmbH) with a
1216 110 min gradient consisting of 2-6% B in 1 min, 6-20% B in 62 min, 20-30% B for 22 min, 30-
1217 60% B in 9 min, 60-90% B for 1 min followed by a hold at 90% B for 5 min. The MS method
1218 consisted of a full MS scan at 60,000 resolution and an AGC target of 3e6 from 350-1800 m/z
1219 followed by MS2 scans collected at 45,000 resolution with an AGC target of 3e6 from 300-1800
1220 m/z followed by MS2 scans collected at 35,000 resolution with an AGC target of 1e5 and 5e4 for
1221 proteome and phosphoprotome fractions, respectively and a maximum injection time of 105 ms.
1222 Dynamic exclusion was set to 15 seconds. The isolation window used for MS2 acquisition was
1223 0.7 m/z and 20 most abundant precursor ions were fragmented with a normalized collision
1224 energy (NCE) of 29 optimized for TMT16 data collection.
1225
1226 Database search and MS/MS quantification for PSD fractions
1227 All the datasets were searched on Spectrum Mill MS Proteomics Software (Broad Institute)
1228 using mouse database downloaded from Uniprot.org on either 12/28/2017 or 04/07/2021
1229 containing 47,069 or 55,734 entrees for 4 weeks and 12 weeks coIP-MS experiments,
1230 respectively[101]. Search parameters included: ESI Qexactive HCD v4 35 scoring parent and
1231 fragment mass tolerance of 20 ppm, 40% minimum matched peak intensity, trypsin allow P
1232 enzyme specificity with up to four missed cleavages, and calculate reversed database scores
1233 enabled. Fixed modifications were carbamidomethylation at cysteine. TMT labeling was
1234 required at lysine, but peptide N-termini could be labeled or unlabeled. Variable modifications
1235 were allowed for protein N-terminal acetylation and oxidized methionine as well as
1236 phosphorylated serine, threonine, and tyrosine for the phosphoproteome datasets. Protein
1237 quantification was achieved by taking the ratio of TMT reporter ions for each sample over the
1238 TMT reporter ion for the median of all channels. TMT16 reporter ion intensities were corrected

1239 for isotopic impurities in the Spectrum Mill protein/peptide summary module using the afRICA
1240 correction method which implements determinant calculations according to Cramer's Rule and
1241 correction factors obtained from the reagent manufacturer's certificate of analysis (Thermo
1242 Fisher Scientific, 90406) for lot numbers VH310017 for both synapse proteomics experiments.
1243 Median normalization was applied to both proteome and phosphoproteome datasets prior to
1244 statistical analysis. Additionally, phosphosite changes were normalized for changes in protein
1245 abundances by fitting a global linear model between the phosphosite and the cognate protein
1246 and extracting the residuals. A moderated two-sample t-test was applied to the datasets to
1247 compare WT, *Akap11*$^{+/-}$ and *Akap11*$^{-/-}$ sample groups. For proteins with multiple isoforms, the
1248 isoform with the greatest abundance (number of spectra observed) was displayed in the plot.
1249
1250 Annotations from Phosphosite Plus
1251 Kinase substrate annotations were downloaded from https://www.phosphosite.org on June 20,
1252 2022. In this database, some kinase substrate sites are inaccurately attributed to a kinase to
1253 which it is indirectly related. For example, Grin2b^{Y1472} is annotated as a PKA Cα substrate in
1254 phopshopsite.org (see Fig. 4b, but is actually a PKC substrate[102]. Similarly, Ctnnb1^{S45} is
1255 annotated as a Gsk3β substrate in phosphosite.org, but is actually a CK1 substrate[46]. These
1256 discrepancies were not adjusted for this manuscript in order to maintain unbiased usage of the
1257 database.
1258
1259 Phosphoproteomics motif analysis
1260 Motif enrichment analysis was performed to generate motif logos using the pyproteome Python
1261 library[103]. Motif logo enrichment values were calculated according to the method described for
1262 pLogo[104]. Peptide 15-mers around each phosphorylation site were generated by Spectrum Mill
1263 "VMsiteFlanks". Foreground and background N-mers were extracted from protein-aligned
1264 sequences, using '-' to pad N-and C-terminal peptides. Quantification values from identical N-
1265 mers (mis-cleaved, oxidized, or multiply-phosphorylated peptides) were combined by taking the
1266 median value. Log odds enrichment values are equal to ($-log\frac{sf(x-1)}{cdf(x)}$), with k = the count of
1267 amino acids at that relative position for phosphosites in a foreground collection ($P < 0.05$; FC >
1268 1.25 or FC < 0.8). Survival function (sf) and cumulative distribution functions (cdf) were
1269 calculated using scipy's hypergeometric distribution model (scipy.stats.hypergeom), with: n =
1270 the total number of foreground N-mers; K = the count of amino acids at that position in the
1271 background collection; and N=the total number of background N-mers.
1272
1273 Immunofluorescence
1274 15-17-week-old male mice were euthanized under isoflurane with transcardial perfusion of ~25
1275 mL with PBS followed by ~25 ml 4% paraformaldehyde (PFA). These mice also underwent an 1
1276 hour open field assays for a separate study[13], at 4 weeks and 12 weeks of age. Brains were
1277 post-fixed overnight in 4% PFA, and washed the next day four times with PBS for 15 min.
1278 Tissues were cryoprotected for 72 hours and stored at 4°C until sectioning. Brains were
1279 sectioned on a vibratome (Leica) at either 40 or 60μm thickness (consistent within technical
1280 replicates) and stored in a freezing buffer (0.1M PBS, 30% ethylene glycol, 30% glycerol, 0.01%
1281 sodium azide).

1282 For immunostaining, free-floating sections were first rinsed 4x with PBS for 10 min. Sections
1283 were blocked and permeabilized with 1 hour RT incubation in a blocking solution. For the first
1284 technical replicate, we used 5% Normal Goat Serum (Sigma, NS02L), with 10% BSA + 0.2%
1285 Triton. For the second technical replicate, we used 5% Normal Donkey Serum (Jackson, 017-
1286 000-121) + 0.2% Triton in PBS for 60 min. Primary antibodies were diluted in blocking solution
1287 and incubated overnight at 4°C, rotating gently. The following day, sections were rinsed 3x for
1288 15 min in PBS containing 0.2% Triton at RT on a shaker. DAPI (Thermo Fisher Scientific,
1289 62248) was added to PBS at a final concentration of 1:5000 (for the first technical replicate) or
1290 1:10,000 (for the second technical replicate) before mounting. The following primary and
1291 secondary antibodies were used: PKA Ca (CST 4782, 1:100), PKA R1a (ThermoFisher MA5-
1292 24981, 1:100). Donkey anti Rabbit 488 (Invitrogen A32790), Donkey anti-Mouse 555 (Invitrogen
1293 A32773), Goat anti Rabbit 488 (Invitrogen A11034), Goat anti-Mouse 555 (Invitrogen A32727).
1294 Whole sections were imaged with a Zeiss Axioscan 7 Slidescanner using exposure and intensity
1295 settings that were constant across samples within technical replicates.
1296
1297 PKA R1α was quantified in FIJI using the freehand selection tool and the intensity measurement
1298 function. Regions were selected using the Allen Brain Atlas as a reference. Experimenters were
1299 blind to conditions during analysis. For representative images, brightness levels were uniformly
1300 increased across the whole images with Zen software (Carl Zeiss) and scaled down to 10% to
1301 accommodate the large field of view of the stitched image.
1302
1303 Tissue collection for RNA sequencing
1304 For bulk and snRNA-seq, mice were harvested between ZT9 and ZT15, near the animals active
1305 period at ZT12. Brain tissues for bulk and snRNA-seq were prepared as described[11], and also
1306 available at protocols.io (https://www.protocols.io/view/fresh-frozenmouse-brain-preparation-for-
1307 single-nu-bcbrism6). At 4 and 12 weeks of age, male WT, *Akap11*$^{+/-}$ and *Akap11*$^{-/-}$ mice were
1308 anesthetized by administration of isoflurane in a gas chamber. Within each age, 4 mice per
1309 genotype were harvested for snRNA-seq, with the exception of 4 week striatum, which had 5
1310 WT samples. For bulk RNA-seq, 5 mice per genotype within an age were collected, with the
1311 exception of the following 4 week samples: *Akap11*$^{+/-}$ SSC and WT Hipp had 6 samples and
1312 *Akap11*$^{-/-}$ str and WT PFC had 4 samples.
1313
1314 Transcardial perfusions were performed with ice-cold Hank's Balanced Salt Solution (HBSS,
1315 Gibco 14175-095) in mice anesthetized with 3% isoflurane delivered continuously via nose
1316 cone. Brains were then frozen gradually over liquid nitrogen vapor and stored at –80°C with
1317 tubes containing O.C.T. (optimal cutting temperature) freezing medium (Tissue-Tek) to prevent
1318 desiccation. Brain region microdissections were performed by hand in a cryostat (Leica
1319 CM3050S), with a ophthalmic microscalpel (Feather safety razor P-715) or 1.5 mm diameter
1320 biopsy punch (Integra 33-31A). PFC, Hipp and SSC were excised by hand. SN and Thal were
1321 collected by biopsy punch. For snRNA-seq studies, both dorsal and ventral striatum were
1322 collected together with a microscalpel, while for bulk RNA-seq, dorsal striatum was collected by
1323 punch. All brain regions were identified according to the Allen Brain Atlas. Dissected tissues
1324 were placed into a precooled 1.5-ml PCR tube and stored at –80°C.
1325

1326 RNA extraction and bulk RNA-seq library preparation RNA was prepared from micro-dissected
1327 tissues using RNeasy Mini Kit (Qiagen, 74106) following the manufacturer's instructions. Briefly,
1328 tissue samples were lysed and homogenized, placed into columns, and bound to the RNeasy
1329 silica membrane. Next, contaminants were washed away. Columns were treated with DNase
1330 (Qiagen) to digest residual DNA and concentrated RNA was eluted in water. RNA concentration
1331 was measured using a NanoDrop Spectrophotometer and RNA integrity (RIN) with RNA pico
1332 chips (Agilent) using a 2100 Bioanalyzer Instrument (Agilent). Purified RNA was stored at -80°C
1333 until library preparation for bulk RNA-seq analysis. Bulk RNA-seq libraries were prepared using
1334 a TruSeq Stranded mRNA Kit (Illumina) following the manufacturer's instructions. 200 ng of
1335 isolated total RNA from each sample was used and the concentration of resulting cDNA library
1336 was measured with High Sensitivity DNA chips (Agilent) using a 2100 Bioanalyzer Instrument
1337 (Agilent). A 10 nM normalized library was pooled, and sequencing was performed on a
1338 NovaSeq S2 (Illumina) with 50 bases each for reads 1 and 2 and 8 bases each for index reads
1339 1 and 2.
1340
1341 For snRNA-seq library preparation, brain tissue dissection and nuclei extraction were performed
1342 within 16 hours to avoid desiccation and freeze-thaw cycles. A gentle, detergent-based
1343 dissociation was used to extract the nuclei, according to a previously published protocol [105] also
1344 available at protocols.io (https://www.protocols.io/view/frozen-tissue-nuclei-extraction-bbseinbe).
1345 Extracted nuclei were then loaded into the 10x Chromium V3.1 system (10x Genomics) and
1346 library preparation was performed according to the manufacturer's protocol. A 10 nM normalized
1347 library was pooled, and sequencing was performed on a NovaSeq S2 (Illumina) with 28 and 75
1348 bases for reads 1 and 2, respectively, and 10 bases each for index reads 1 and 2.
1349
1350 Bulk RNA-seq DE analysis
1351 FASTQ files were aligned to a reference, which was derived from the genome FASTA file and
1352 transcriptome GTF extracted from the CellRanger mm10 reference. Alignment and
1353 quantification were performed using a Nextflow V1 pipeline[106]
1354 (https://github.com/seanken/BulkIsoform/blob/main/Pipeline). Quantification was performed by
1355 Salmon[107] (version 1.7.0, with arguments -l A --posBias --seqBias --gcBias --validateMapping),
1356 using a Salmon reference built with the salmon index command with genomic decoys included.
1357 Two samples - HP_HT_941 and TH_WT_913 - were removed from analysis due to evidence of
1358 contamination by aberrant marker gene expression.
1359
1360
1361
1362
1363
1364
1365
1366
1367
1368

Dataset	WT sample size (*n*)	*Akap11*$^{+/-}$ sample size (*n*)	*Akap11*$^{-/-}$ sample size (*n*)
4wk PFC (Prefrontal Cortex)	5	6	5
4wk Hipp (Hippocampus)	6	4	5
4wk SSC (Somatosensory Cortex)	5	6	5
4wk Striatum (Str)	5	5	5
4wk Thalamus (Thal)	5	5	5
4wk Substantia Nigra (SN)	6	6	5
12wk PFC	5	5	5
12wk Hipp	5	5	5
12wk SSC	5	5	5
12wk Str	5	5	5
12wk Thal	5	5	5
12wk SN	5	5	5

Differential expression:
Differential expression analysis was performed to compare the heterozygous or knockout mutants to the wild-type mice for each brain region and age using the Wald test in R package DESeq2[108] (version 1.34). Salmon output was loaded using R package tximport[109] (version 1.22). Genes that had less than 10 counts across all samples in each experiment were removed from our analysis. Due to evidence of dissection variability in striatum by excitatory marker genes, DESeq2's PC1 was added as a covariate for differential expression in 1 month striatum. Log2 fold change shrinkage was applied using the "normal" shrinkage estimator in DESeq2. DESeq2's default results filtering was used and all genes in a given comparison with padj = NA were removed from downstream analysis. For 1 month hippocampus and thalamus, the default filtering removed the majority of genes, so we changed the filtering for the heterozygous vs. WT comparison to match the less aggressive filtering in the knockout vs. WT comparison.

Single-nucleus RNA-seq analysis
snRNA-seq reads were aligned to an mm10 mouse reference genome containing introns (https://cf.10xgenomics.com/supp/cell-exp/refdata-gex-mm10-2020-A.tar.gz) using the Cell Ranger v3.0.2 pipeline (10x Genomics)[110]. Cell Ranger count was run with default parameters and the following additional flags: --chemistry=SC3Pv3 and --expect-cells=15000. Replicates for the 4-week STR dataset were down-sampled to contain the same number of reads per cell using Cell Ranger aggr with default parameters.

1390
1391 Seurat v4.0.3[111] was used to analyze Unique Molecular Identifier (UMI) counts. Nuclei
1392 expressing less than 500 genes were removed and the remaining nuclei were normalized by
1393 total expression, multiplied by ten thousand, and log transformed. The data were then scaled
1394 using Seurat's ScaleData function. Seurat's RunPCA function was used to perform linear
1395 dimension reduction on the variable genes within the scaled data. Clustering in the PCA space
1396 was then run using Seurat's FindNeighbors and FindClusters functions and the clusters were
1397 visualized using Seurat's RunUMAP function. Doublet identification was performed using the
1398 Scrublet v0.2.3[112]. Python package with default parameters. Clusters and nuclei with a scrublet
1399 score above the region-specific thresholds were determined to be doublets and were removed
1400 from the data. The table below shows the used scrublet score thresholds for all snRNA-seq
1401 datasets:
1402

Dataset	Scrublet Score Threshold
4wk PFC	0.36
4wk Striatum	0.2
12wk PFC	0.4
12wk Striatum	0.4

1403
1404 Cluster cell type assignment was evaluated using region-specific cell type marker genes.
1405 Neuronal subtypes were identified by re-clustering the nuclei of a given major cell type and
1406 evaluating expression of subtype-specific marker genes. Marker genes for the more widely
1407 classified major cell types and subtypes were identified in the literature[113]. Rarer cell types and
1408 subtypes were identified using Seurat's FindMarkers function. The clusters were then identified
1409 by searching cluster-specific marker genes on mouseBrain.org[114] and or dropviz.org[115].
1410

Dataset	WT sample size (*n*)	*Akap11*$^{+/-}$ sample size (*n*)	*Akap11*$^{-/-}$ sample size (*n*)
4wk PFC	4	4	4
4wk Striatum	4	4	4
12wk PFC	4	4	4
12wk Striatum	5	4	4

1411
1412
1413 Pseudobulk DE analysis
1414 snRNA-seq differential expression (DE) analysis was performed using the pseudobulk
1415 approach. For each dataset, counts were grouped by cell type and replicate, then gene counts
1416 were summed across each replicate within a cell type, resulting in one count value per replicate
1417 per cell type. Surrogate variable analysis (SVA) was conducted using the sva v3.42.0 R
1418 package[116] to account for unknown sources of variation within each experiment. Differential

expression analysis was then run with the covariates identified by SVA using the EdgeR v3.22.3 R package[117]. DEGs were defined as genes with a Benjamini-Hochberg adjusted *P*-value <0.05.

Gene set enrichment analysis

GSEA was performed with the R Bioconductor package *fgsea*[118] using C5 ontology gene sets obtained from the Molecular signatures database (MSigDB) on September 28, 2022. Genes were pre-ranked using their test-statistics within each comparison, and their *Homo sapiens* homolog-associated were used for the analysis. For genes or proteins with multiple isoforms, the isoform with the largest effect-size (absolute value of the t-statistic) was used for pre-ranking. Because the enrichment analyses were carried out using the proteins' gene symbols, we use the terms gene set and protein set interchangeably in this study. For each of these gene sets, mouse gene symbols from transcriptomics and proteomics results were mapped to matching *Homo sapiens* homolog-associated gene symbols through annotations extracted from Ensembl's BioMart data service; the human symbols were then used to perform GSEA. A list of all significant GO terms (FDR < 0.05) for all datasets are provided in Supplementary Tables. GSEA analysis with custom gene sets was conducted by appending these sets to the C5 MSigDB database.

Curated gene sets

Phosphosites that correlate with homeostatic synaptic scaling were curated from Desch et al.[60], including together all phosphosites that were significantly altered (adjusted *P*-value < 0.05) after 5 minutes, 15 minutes or 24 hours of either bicuculline or tetrodotoxin treatment. Curated gene sets that we have previously described[11] include "Activity-regulated genes" (ARGs), which include rapid, delayed and slow primary response genes induced by neuronal depolarization *in vitro*[70], GWAS and exome associations for neuropsychiatric traits[26,71–73], and dopamine-induced genes which are genes with FDR < 0.1 that were upregulated in striatal neuronal culture following 1 hour dopamine treatment[119].

Brain slice electrophysiology

6-8-week-old male and female mice were used for brain slice electrophysiology experiments, including n = 9 slices from 4 mice WT, and n = 8 slices from 4 mice *Akap11*$^{-/-}$ for input-output experiments; n = 25 slices from 8 mice WT, n = 24 slices from 7 mice *Akap11*$^{+/-}$, and n = 23 slices from 8 mice *Akap11*$^{-/-}$ for early LTP and paired-pulse facilitation experiments. An NMDG-based cutting solution was used and contains (in Mm): 93 NMDG, 2.5 KCl, 1.2 NaH_2PO_4, 30 $NaHCO_3$, 20 HEPES, 25 Glucose, 10 $MgSO_4$, 0.5 $CaCl_2$, 5 Sodium Ascorbate, 2 Thiourea, 3 Sodium Pyruvate. pH = 7.3-7.4, OSM = 300-310. The external artificial cerebrospinal fluid (ACSF) recording solution contains(in Mm): 124 NaCl, 2.5 KCl, 1.25 NaH_2PO_4, 24 $NaHCO_3$, 5 HEPES, 12.5 Glucose,1 $MgSO_4$, 2 $CaCl_2$ pH = 7.35, OSM = 300. For brain slice preparation, cardiac perfusion was performed with cold NMDG cutting solution under isoflurane anesthesia. Transverse (horizontal) brain slices containing hippocampus were cut at 400μM with a Leica VT1200S Microtome when submerged in ice-cold NMDG cutting solution. Brain slices were transferred to NMDG solution at 32ºC for approximately 10 min before being transferred to RT brain slice holding solution. Slices were allowed to recover for at least 1 hour before starting the recordings.

1463 To obtain hippocampus field electric postsynaptic potential (EPSP), a concentric bipolar stim
1464 electrode (FHC Inc) and a borosilicate glass recording electrode (2-3mOhm resistance) were
1465 placed in the classic schaffer collateral to CA1 (SC-CA1) pathway. The signals were low-pass
1466 filtered at 2.8kHz using a MultiClamp 700B amplifier (Molecular Devices) and digitized at 10kHz
1467 using a DAQ board (National Instrument). Baseline field EPSP were evoked by a paired-pulse
1468 stimulation (40ms ISI) every twenty seconds, and a stimulation intensity that evoked 40% of the
1469 maximum field EPSP response was used for baseline recording.
1470
1471 For input-output recordings, field EPSP responses were evoked with varying stimulation
1472 intensities (20-500 μA). For early LTP recordings, slices were stimulated for approximately 30
1473 mins until a stable baseline field EPSP was obtained. Theta burst stimulation consists of short
1474 bursts of 4 stimulation pulses at 10Hz delivered at theta frequency (5Hz, 10 epochs) were used
1475 to induce LTP. The field EPSP was recorded for another 20 mins after LTP induction. Paired-
1476 pulse ratio was quantified using the field EPSP collected from the 10-minute period before LTP
1477 induction and was defined as the ratio between the second and the first field EPSP slope. Field
1478 EPSP slope was quantified as the slope during 10-90% of the raise time.
1479
1480 Single-molecule fluorescent in-situ hybridization (smFISH)
1481 Mouse brain characterization of *Akap11*, *Prkaca*, and *Prkar1a* expression was performed using
1482 Advanced Cell System's (ACD) single-molecule *in situ* hybridization multiplexed fluorescent
1483 amplification kits (ACD catalog numbers 323270). 12-week-old male mice, n=6 per genotype
1484 WT, *Akap11*$^{+/-}$, and *Akap11*$^{-/-}$, were deeply anesthetized under isoflurane, perfused with ice-cold
1485 HBSS for 3 minutes, and decapitated. Brains were extracted and frozen gradually over liquid
1486 nitrogen vapors. Frozen brains were stored in tubes with O.C.T. in -80°c. Brains were sectioned
1487 sagittally at 12um/section using a Leica cryostat. Four sections per animal (two sections per
1488 slide) were collected on SuperFrost Charged slides and stored at -80ºC and smFISH was
1489 performed the following day. Slides were post-fixed in freshly made, pre-chilled 4% PFA
1490 (Electron Microscopy Sciences) in PBS for 1 hour on ice. Sections were then dehydrated with
1491 50%, 70%, and 100% ethanol for 5 min at room temperature. All slides were outlined with a
1492 grease pen and all following smFISH steps were done on a humidified slide rack. Sections were
1493 then treated with hydrogen peroxide for 10 min followed by three PBS washes. Sections then
1494 underwent permeabilization with "protease IV" for 30 min followed by three PBS washes.
1495 Sections were then hybridized using probes to *Prkaca* (channel 1), *Akap11* (channel 2), and
1496 *Prkar1a* (channel 3) at 40ºC for 2 hours, washed twice with wash buffer, and placed in
1497 aluminum foil-wrapped slide holders filled with 5X SSC (Thermo Fisher Scientific, 15557044)
1498 overnight at room temperature. The following day, sections were thoroughly washed in wash
1499 buffer and probes were amplified using the AMP reagents from the ACD kit. Slides were
1500 washed between each step using the wash buffer. HRP binding was also carried out according
1501 to the kit's protocol with C1, C2, and C3. Fluorophores were diluted at 1:750 in TSA buffer: C1
1502 was in 488; Channel 2 was in Cy3; Channel 3; Cy5. Once the procedure was completed, slides
1503 were counterstained with room temperature Prolong Gold Antifade Mountant with DAPI (Thermo
1504 Fisher Scientific, P36935).
1505

1506 Slides were scanned in a Zeiss Axioscan 7 microscope slide scanner with a 40x objective
1507 quadruple bandpass filter set with DAPI focus. CZI files were converted to 8-bit TIFF images in
1508 FIJI and appropriate brain regions (cortex, thalamus, hippocampus, and striatum) were outlined
1509 using the freehand selection tool. To assess levels of *Akap11*, *Prkaca*, and *Prka1a*, the mean
1510 intensity was quantified for each outlined brain region with background subtraction using the
1511 declive (VI), molecular layer. Four sections per animal were averaged and normalized to the WT
1512 to minimize batch effects.
1513
1514 Viruses
1515 FLIM-AKAR and FLIM-AKAR^{T391A} viruses were packaged in-house into a AAV2/AAV9 vector
1516 using plasmids that were available from Addgene (no. 60445 and 60446). The final viral
1517 constructs and concentration used in this study were: AAV2/1-FLEX-FLIM-AKAR (8.53 ×
1518 10^{12}gc/ml), AAV9-FLEX-FLIM-AKAR (2.14 × 10^{13} gc/ml), AAV2-FLEX-FLIM-AKAR^{T391A} (1.23 x
1519 10^13 gc/ml), AAV9-FLEX-FLIM-AKAR^{T391A} (7.67 × 10^{12} gc/ml). AAV2rg-Ef1a-Cre (1.39 × 10^{13}
1520 gc/ml) was obtained from Salk institute. While both AAV2 and AAV9 versions of the FLIM-AKAR
1521 and FLIM-AKAR^{T391A} were used in this study, we saw no noticeable difference in their
1522 expression level and baseline fluorescence lifetime when expressed in wild-type mice. During
1523 the experiments, FLIM-AKAR or mutant FLIM-AKAR^{T391A} virus was mixed with the Cre virus in a
1524 4:1 ratio. A final volume of 250 nL was used for intracranial injection.
1525
1526 Stereotaxic Surgery and Virus Injection
1527 Mice were anesthetized with isoflurane and underwent bilateral injection of the virus mix (FLIM-
1528 AKAR + Cre or FLIM-AKAR^{T391A} + Cre). Typically, one side of the brain is injected with FLIM-
1529 AKAR + Cre, while the other side is injected with FLIM-AKAR^{T391A} + Cre while counterbalancing
1530 the sides of the brain, with the exception of twelve mice (mixed genotypes) injected with Dlight
1531 3.8 virus instead of FLIM-AKAR^{T391A} + Cre (data not included). Virus injection was conducted
1532 using coordinates for the nucleus accumbens lateral shell (AP +1.20, ML ±1.50 from bregma,
1533 DV -4.2 from brain surface). Optical fibers (MFC_200/230-0.37_4.5mm_MF1.25_FLT from Doris
1534 Lenses) were placed bilaterally and ~ 0.3 mm above the injection site.
1535
1536 Fluorescence lifetime photometry (FLiP)
1537 Thirty-three 12-20 week-old *Akap11* mutant mice of mixed genotypes were used for stereotaxic
1538 surgeries and subsequent FLiP measurements, including baseline, D1R antagonist and D2R
1539 antagonist expriments. Approximately equal number of male and female mice were used (n=10
1540 WT, n=11 *Akap11*$^{+/-}$ and n=10 *Akap11*$^{-/-}$). The fluorescence lifetime and intensity of the FILM-
1541 AKAR (or FLIM-AKAR^{T391A}) was measured in real time at 10kHz using a Fluorescent lifetime
1542 photometry system[95]. Customized MATLABM software was used to collect the lifetime
1543 measurement, and the lifetime data was down sampled to 10 Hz using a rolling mean. This
1544 setup will be described in detail and analysis code will be provided in an upcoming manuscript
1545 (Lodder *et al.,* In Preparation).
1546
1547 Animals were habituated into the recording room for at least 30 mins before the experiments.
1548 Baseline FLIM-AKAR lifetime was measured for 20 mins during the first measurement, and
1549 were then collected for 10 mins each during subsequent measurements, while animals were

1550 allowed to freely move in an open field (18x18 cm). Drug injections (dopamine D1/D2
1551 antagonists) during pharmacology experiments were conducted after 10 mins baseline lifetime
1552 measurement, and the lifetime data were collected for at least another 20 mins following
1553 intraperitoneal injections.
1554
1555 The drugs used in our study include: D1R antagonist (SKF 83566 hydrobromide, Cayman
1556 Chemical #29480; 3 mg kg^{-1}), D2R antagonist (eticlopride hydrochloride, Cayman Chemical
1557 #29112; 0.5 mg kg^{-1}). Drugs were dissolved in sterile saline at appropriate concentrations and
1558 were injected at 0.1 ml solution per 10 g of mouse. An average injection including scruffing the
1559 mice took ~30 s and animals were habituated to the injection procedure with sterile saline twice
1560 before the pharmacology experiments.
1561
1562 After the FLiP experiments were completed, all mice were perfused transcardially with PFA.
1563 Coronal brain sections (80μM) near the optical fiber implants were sliced using a vibratome
1564 (Leica VT1200S). The brain slices were mounted with Prolong Gold Antifade Mountant with
1565 DAPI (Thermo Fisher Scientific, P36935) and imaged with a Zeiss Axioscan 7 slidescanner.
1566
1567 The experimenter was blinded to the genotype of the mice during the experiments and
1568 subsequent data analysis. Two out of thirty-three FLIM-AKAR measurements were excluded
1569 from the study due to the low expression of the FILM-AKAR causing the autofluorescent
1570 contribution to the recorded lifetime to be greater than 20% based on our estimation. The
1571 exclusion criteria was determined before the experiment while the experimenter was still blinded
1572 to the mice genotypes.
1573
1574 Amphetamine induced-hyperlocomotion (AIH)
1575 *Akap11* mice that were 10-12 weeks old with roughly equal numbers of male and female mice
1576 were used for the AIH experiment. n=18 WT, n=22 *Akap11*$^{+/-}$ and n=14 *Akap11*$^{-/-}$ were used for
1577 this experiment. Mice in each genotype were randomly assigned to the saline or amphetamine
1578 groups. Before the experiment, dextroamphetamine sulfate (Millipore Sigma 1180004; salt
1579 corrected) was dissolved in water at 0.2667 mg/mL and was pH corrected to 7.3. Mice were
1580 weighted and were allowed to habituate in the behavioral room (under white light) for 30 mins
1581 before the start of the experiment. For the measurement of locomotion, mice were placed in
1582 Omnitech Electronics Inc SuperFlex Open Field apparatus, which was cleaned with 70%
1583 ethanol between each experiment. First, a 90 min baseline locomotion was recorded, followed
1584 by subcutaneous injection of amphetamine at a dose of 2mg/kg or saline. Following drug
1585 injection, the locomotion data were collected for another 90 min. Locomotion data were
1586 measured by infrared beams and were measured by beam breaks, and were grouped into 5-min
1587 bins for analysis.
1588
1589 Statistics
1590 Statistics for immunoblots, fluorescence lifetime photometry (FLiP), and AIH were calculated in
1591 GraphPad Prism, with each dot representing an individual animal. Immunoblots and FLiP
1592 experiments including the genotype factor and a second factor (Age, Brain region, Protein

1593 interactor, or FLIM-AKAR variant) were quantified with two-way ANOVA. For all analyses with a
1594 significant main effect of genotype, post hoc Tukey's multiple comparisons were conducted for
1595 all possible comparisons within the same level of the second factor (e.g. WT, *Akap11*$^{+/-}$ and
1596 *Akap11*$^{-/-}$ were compared within one age, but not between different ages). Multiple comparisons
1597 were conducted with Tukey's post hoc test. For Extended Data Figs. 2b,c and 3g, where
1598 *Akap11*$^{-/-}$ was excluded, Sidak's multiple comparisons test was used. For immunoblot, and FLiP
1599 experiments where genotype was the only variable, statistically analysis were conducted by
1600 one-way ANOVA followed by Tukey's post hoc test to compare all genotype pairs. Further
1601 statistical information are available in Supplementary Table 1.
1602
1603 Data availability
1604 The original mass spectra and the protein sequence database used for searches have been
1605 deposited in the public proteomics repository MassIVE (http://massive.ucsd.edu)
1606 and are accessible at ftp://MSV000095852@massive.ucsd.edu. These datasets will be made
1607 public upon acceptance of the manuscript. Processed and raw bulk and single nucleus RNA
1608 sequencing data have been deposited at Gene Expression Omnibus (GEO) with the following
1609 IDs: bulk RNAseq: GSE272097. single nucleus RNAseq: GSE272098. For analyses of *Akap11*
1610 transcript abundance in wild-type mice, the following publicly available datasets were
1611 analyzed: GSE218573. All software used in the analysis are publicly available.

1612 **References**

1613 1. Ferrari, A. J. *et al.* The prevalence and burden of bipolar disorder: findings from the Global Burden of Disease
1614 Study 2013. *Bipolar Disord.* **18**, 440–450 (2016).
1615 2. McGrath, J., Saha, S., Chant, D. & Welham, J. Schizophrenia: a concise overview of incidence, prevalence, and
1616 mortality. *Epidemiol. Rev.* **30**, 67–76 (2008).
1617 3. Polderman, T. J. C. *et al.* Meta-analysis of the heritability of human traits based on fifty years of twin studies.
1618 *Nat. Genet.* **47**, 702–709 (2015).
1619 4. Jauhar, S., Johnstone, M. & McKenna, P. J. Schizophrenia. *Lancet* **399**, 473–486 (2022).
1620 5. Singh, T. *et al.* Rare coding variants in ten genes confer substantial risk for schizophrenia. *Nature* **604**, 509–516
1621 (2022).
1622 6. Palmer, D. S. *et al.* Exome sequencing in bipolar disorder identifies AKAP11 as a risk gene shared with
1623 schizophrenia. *Nat. Genet.* **54**, 541–547 (2022).
1624 7. Trubetskoy, V. *et al.* Mapping genomic loci implicates genes and synaptic biology in schizophrenia. *Nature* **604**,
1625 502–508 (2022).
1626 8. Mullins, N. *et al.* Genome-wide association study of more than 40,000 bipolar disorder cases provides new
1627 insights into the underlying biology. *Nat. Genet.* **53**, 817–829 (2021).
1628 9. Liu, D. *et al.* Schizophrenia risk conferred by rare protein-truncating variants is conserved across diverse human

1629 populations. *Nat. Genet.* **55**, 369–376 (2023).
1630 10. Chen, R. *et al.* Cell type-specific mechanism of Setd1a heterozygosity in schizophrenia pathogenesis. *Sci Adv*
1631 **8**, eabm1077 (2022).
1632 11. Farsi, Z. *et al.* Brain-region-specific changes in neurons and glia and dysregulation of dopamine signaling in
1633 Grin2a mutant mice. *Neuron* **111**, 3378-3396.e9 (2023).
1634 12. Katrancha, S. M. *et al.* Trio Haploinsufficiency Causes Neurodevelopmental Disease-Associated Deficits. *Cell*
1635 *Rep.* **26**, 2805-2817.e9 (2019).
1636 13. Herzog, L. E. *et al.* Mouse mutants in schizophrenia risk genes GRIN2A and AKAP11 show EEG abnormalities
1637 in common with schizophrenia patients. *Transl. Psychiatry* **13**, 92 (2023).
1638 14. Wong, W. & Scott, J. D. AKAP signalling complexes: focal points in space and time. *Nat. Rev. Mol. Cell Biol.* **5**,
1639 959–970 (2004).
1640 15. Day, M. E. *et al.* Isoform-specific targeting of PKA to multivesicular bodies. *J. Cell Biol.* **193**, 347–363 (2011).
1641 16. Lester, L. B., Coghlan, V. M., Nauert, B. & Scott, J. D. Cloning and Characterization of a Novel A-kinase
1642 Anchoring Protein: AKAP 220, ASSOCIATION WITH TESTICULAR PEROXISOMES (∗). *J. Biol. Chem.* **271**,
1643 9460–9465 (1996).
1644 17. Tanji, C. *et al.* A-kinase anchoring protein AKAP220 binds to glycogen synthase kinase-3beta (GSK-3beta) and
1645 mediates protein kinase A-dependent inhibition of GSK-3beta. *J. Biol. Chem.* **277**, 36955–36961 (2002).
1646 18. Schillace, R. V. & Scott, J. D. Association of the type 1 protein phosphatase PP1 with the A-kinase anchoring
1647 protein AKAP220. *Curr. Biol.* **9**, 321–324 (1999).
1648 19. Logue, J. S. *et al.* AKAP220 protein organizes signaling elements that impact cell migration. *J. Biol. Chem.* **286**,
1649 39269–39281 (2011).
1650 20. Yang, L., Nakayama, Y., Hattori, N., Liu, B. & Inagaki, C. GABAC-Receptor Stimulation Activates cAMP-
1651 Dependent Protein Kinase via A-Kinase Anchoring Protein 220. *J. Pharmacol. Sci.* **106**, 578–584 (2008).
1652 21. Mikitova, V. & Levine, T. P. Analysis of the key elements of FFAT-like motifs identifies new proteins that
1653 potentially bind VAP on the ER, including two AKAPs and FAPP2. *PLoS One* **7**, e30455 (2012).
1654 22. Deng, Z. *et al.* Selective autophagy of AKAP11 activates cAMP/PKA to fuel mitochondrial metabolism and
1655 tumor cell growth. *Proc. Natl. Acad. Sci. U. S. A.* **118**, (2021).
1656 23. Whiting, J. L. *et al.* AKAP220 manages apical actin networks that coordinate aquaporin-2 location and renal
1657 water reabsorption. *Proc. Natl. Acad. Sci. U. S. A.* **113**, E4328-37 (2016).
1658 24. Whiting, J. L. *et al.* Protein Kinase A Opposes the Phosphorylation-dependent Recruitment of Glycogen
1659 Synthase Kinase 3β to A-kinase Anchoring Protein 220*. *J. Biol. Chem.* **290**, 19445–19457 (2015).

1660 25. Dema, A. *et al.* The A-Kinase Anchoring Protein (AKAP) Glycogen Synthase Kinase 3β Interaction Protein
1661 (GSKIP) Regulates β-Catenin through Its Interactions with Both Protein Kinase A (PKA) and GSK3β *. *J. Biol.*
1662 *Chem.* **291**, 19618–19630 (2016).
1663 26. Satterstrom, F. K. *et al.* Large-Scale Exome Sequencing Study Implicates Both Developmental and Functional
1664 Changes in the Neurobiology of Autism. *Cell* **180**, 568-584.e23 (2020).
1665 27. Shih, Y.-T., Alipio, J. B. & Sahay, A. An inhibitory circuit-based enhancer of DYRK1A function reverses Dyrk1a-
1666 associated impairment in social recognition. *Neuron* **111**, 3084-3101.e5 (2023).
1667 28. Dang, T. *et al.* Autism-associated Dyrk1a truncation mutants impair neuronal dendritic and spine growth and
1668 interfere with postnatal cortical development. *Mol. Psychiatry* **23**, 747–758 (2018).
1669 29. Levy, J. A., LaFlamme, C. W., Tsaprailis, G., Crynen, G. & Page, D. T. Dyrk1a Mutations Cause Undergrowth of
1670 Cortical Pyramidal Neurons via Dysregulated Growth Factor Signaling. *Biol. Psychiatry* **90**, 295–306 (2021).
1671 30. Arranz, J. *et al.* Impaired development of neocortical circuits contributes to the neurological alterations in
1672 DYRK1A haploinsufficiency syndrome. *Neurobiol. Dis.* **127**, 210–222 (2019).
1673 31. Vierra, N. C. *et al.* Neuronal ER-plasma membrane junctions couple excitation to Ca2+-activated PKA signaling.
1674 *Nat. Commun.* **14**, 1–16 (2023).
1675 32. Subramanian, A. *et al.* Gene set enrichment analysis: A knowledge-based approach for interpreting genome-
1676 wide expression profiles. *Proceedings of the National Academy of Sciences* **102**, 15545–15550 (2005).
1677 33. Parzych, K. R. & Klionsky, D. J. An overview of autophagy: morphology, mechanism, and regulation. *Antioxid.*
1678 *Redox Signal.* **20**, 460–473 (2014).
1679 34. Segura-Roman, A. *et al.* Autophagosomes coordinate an AKAP11-dependent regulatory checkpoint that shapes
1680 neuronal PKA signaling. *bioRxiv* 2024.08.06.606738 (2024) doi:10.1101/2024.08.06.606738.
1681 35. Kandel, E. R. The molecular biology of memory: cAMP, PKA, CRE, CREB-1, CREB-2, and CPEB. *Mol. Brain* **5**,
1682 14 (2012).
1683 36. Solmi, M. *et al.* Age at onset of mental disorders worldwide: large-scale meta-analysis of 192 epidemiological
1684 studies. *Mol. Psychiatry* **27**, 281–295 (2022).
1685 37. Darling, N. J. & Cohen, P. Nuts and bolts of the salt-inducible kinases (SIKs). *Biochem. J* **478**, 1377–1397
1686 (2021).
1687 38. Yamada, T., Sakisaka, T., Hisata, S., Baba, T. & Takai, Y. RA-RhoGAP, Rap-activated Rho GTPase-activating
1688 protein implicated in neurite outgrowth through Rho. *J. Biol. Chem.* **280**, 33026–33034 (2005).
1689 39. Aryal, S. *et al.* Deep proteomics identifies shared molecular pathway alterations in synapses of patients with
1690 schizophrenia and bipolar disorder and mouse model. *Cell Rep.* **42**, 112497 (2023).

1691 40. Koopmans, F. *et al.* SynGO: An Evidence-Based, Expert-Curated Knowledge Base for the Synapse. *Neuron*
1692 **103**, 217-234.e4 (2019).
1693 41. Hornbeck, P. V. *et al.* PhosphoSitePlus, 2014: mutations, PTMs and recalibrations. *Nucleic Acids Res.* **43**,
1694 D512-20 (2015).
1695 42. Bramson, H. N., Kaiser, E. T. & Mildvan, A. S. Mechanistic studies of cAMP-dependent protein kinase action.
1696 *CRC Crit. Rev. Biochem.* **15**, 93–124 (1984).
1697 43. Krug, K. *et al.* A Curated Resource for Phosphosite-specific Signature Analysis. *Mol. Cell. Proteomics* **18**, 576–
1698 593 (2019).
1699 44. Lisman, J., Yasuda, R. & Raghavachari, S. Mechanisms of CaMKII action in long-term potentiation. *Nat. Rev.*
1700 *Neurosci.* **13**, 169–182 (2012).
1701 45. Liu, C. *et al.* Control of beta-catenin phosphorylation/degradation by a dual-kinase mechanism. *Cell* **108**, 837–
1702 847 (2002).
1703 46. Amit, S. *et al.* Axin-mediated CKI phosphorylation of beta-catenin at Ser 45: a molecular switch for the Wnt
1704 pathway. *Genes Dev.* **16**, 1066–1076 (2002).
1705 47. Fang, X. *et al.* Phosphorylation and inactivation of glycogen synthase kinase 3 by protein kinase A. *Proc. Natl.*
1706 *Acad. Sci. U. S. A.* **97**, 11960–11965 (2000).
1707 48. Malhi, G. S., Gessler, D. & Outhred, T. The use of lithium for the treatment of bipolar disorder:
1708 Recommendations from clinical practice guidelines. *J. Affect. Disord.* **217**, 266–280 (2017).
1709 49. Nakao, K. *et al.* GSK3β inhibition restores cortical gamma oscillation and cognitive behavior in a mouse model
1710 of NMDA receptor hypofunction relevant to schizophrenia. *Neuropsychopharmacology* **45**, 2207–2218 (2020).
1711 50. Banke, T. G. *et al.* Control of GluR1 AMPA receptor function by cAMP-dependent protein kinase. *J. Neurosci.*
1712 **20**, 89–102 (2000).
1713 51. Ehlers, M. D. Reinsertion or degradation of AMPA receptors determined by activity-dependent endocytic
1714 sorting. *Neuron* **28**, 511–525 (2000).
1715 52. Esteban, J. A. *et al.* PKA phosphorylation of AMPA receptor subunits controls synaptic trafficking underlying
1716 plasticity. *Nat. Neurosci.* **6**, 136–143 (2003).
1717 53. Diering, G. H., Gustina, A. S. & Huganir, R. L. PKA-GluA1 coupling via AKAP5 controls AMPA receptor
1718 phosphorylation and cell-surface targeting during bidirectional homeostatic plasticity. *Neuron* **84**, 790–805
1719 (2014).
1720 54. Huganir, R. L. & Nicoll, R. A. AMPARs and synaptic plasticity: the last 25 years. *Neuron* **80**, 704–717 (2013).
1721 55. Nagy, G. *et al.* Regulation of releasable vesicle pool sizes by protein kinase A-dependent phosphorylation of

1722 SNAP-25. *Neuron* **41**, 417–429 (2004).
1723 56. Simsek-Duran, F., Linden, D. J. & Lonart, G. Adapter protein 14-3-3 is required for a presynaptic form of LTP in
1724 the cerebellum. *Nat. Neurosci.* **7**, 1296–1298 (2004).
1725 57. Lonart, G. *et al.* Phosphorylation of RIM1alpha by PKA triggers presynaptic long-term potentiation at cerebellar
1726 parallel fiber synapses. *Cell* **115**, 49–60 (2003).
1727 58. Kaeser, P. S. *et al.* RIM1alpha phosphorylation at serine-413 by protein kinase A is not required for presynaptic
1728 long-term plasticity or learning. *Proc. Natl. Acad. Sci. U. S. A.* **105**, 14680–14685 (2008).
1729 59. Betzenhauser, M. J., Fike, J. L., Wagner, L. E., 2nd & Yule, D. I. Protein kinase A increases type-2 inositol
1730 1,4,5-trisphosphate receptor activity by phosphorylation of serine 937. *J. Biol. Chem.* **284**, 25116–25125 (2009).
1731 60. Desch, K., Langer, J. D. & Schuman, E. M. Dynamic bi-directional phosphorylation events associated with the
1732 reciprocal regulation of synapses during homeostatic up- and down-scaling. *Cell Rep.* **36**, 109583 (2021).
1733 61. Diering, G. H. & Huganir, R. L. The AMPA Receptor Code of Synaptic Plasticity. *Neuron* **100**, 314–329 (2018).
1734 62. Makino, Y., Johnson, R. C., Yu, Y., Takamiya, K. & Huganir, R. L. Enhanced synaptic plasticity in mice with
1735 phosphomimetic mutation of the GluA1 AMPA receptor. *Proceedings of the National Academy of Sciences* **108**,
1736 8450–8455 (2011).
1737 63. Dejanovic, B., Sheng, M. & Hanson, J. E. Targeting synapse function and loss for treatment of
1738 neurodegenerative diseases. *Nat. Rev. Drug Discov.* **23**, 23–42 (2024).
1739 64. Schizophrenia Working Group of the Psychiatric Genomics Consortium. Biological insights from 108
1740 schizophrenia-associated genetic loci. *Nature* **511**, 421–427 (2014).
1741 65. Sekar, A. *et al.* Schizophrenia risk from complex variation of complement component 4. *Nature* **530**, 177–183
1742 (2016).
1743 66. Gandal, M. J. *et al.* Transcriptome-wide isoform-level dysregulation in ASD, schizophrenia, and bipolar disorder.
1744 *Science* **362**, eaat8127 (2018).
1745 67. Ruzicka, B. *et al.* Single-Cell Dissection of Schizophrenia Reveals Neurodevelopmental-Synaptic Link and
1746 Transcriptional Resilience Associated Cellular State. *Biol. Psychiatry* **89**, S106 (2021).
1747 68. Minzenberg, M. J., Laird, A. R., Thelen, S., Carter, C. S. & Glahn, D. C. Meta-analysis of 41 functional
1748 neuroimaging studies of executive function in schizophrenia. *Arch. Gen. Psychiatry* **66**, 811–822 (2009).
1749 69. Chen, C.-H., Suckling, J., Lennox, B. R., Ooi, C. & Bullmore, E. T. A quantitative meta-analysis of fMRI studies
1750 in bipolar disorder: Meta-analysis of fMRI studies in BD. *Bipolar Disord.* **13**, 1–15 (2011).
1751 70. Tyssowski, K. M. *et al.* Different Neuronal Activity Patterns Induce Different Gene Expression Programs. *Neuron*
1752 **98**, 530-546.e11 (2018).

1753 71. Buniello, A. *et al.* The NHGRI-EBI GWAS Catalog of published genome-wide association studies, targeted
1754 arrays and summary statistics 2019. *Nucleic Acids Res.* **47**, D1005–D1012 (2019).
1755 72. Kaplanis, J. *et al.* Evidence for 28 genetic disorders discovered by combining healthcare and research data.
1756 *Nature* **586**, 757–762 (2020).
1757 73. International League Against Epilepsy Consortium on Complex Epilepsies. Genome-wide mega-analysis
1758 identifies 16 loci and highlights diverse biological mechanisms in the common epilepsies. *Nat. Commun.* **9**,
1759 5269 (2018).
1760 74. Cross-Disorder Group of the Psychiatric Genomics Consortium. Genomic Relationships, Novel Loci, and
1761 Pleiotropic Mechanisms across Eight Psychiatric Disorders. *Cell* **179**, 1469-1482.e11 (2019).
1762 75. Ling, E. *et al.* A concerted neuron–astrocyte program declines in ageing and schizophrenia. *Nature* **627**, 604–
1763 611 (2024).
1764 76. Glennon, R. A., Titeler, M. & McKenney, J. D. Evidence for 5-HT2 involvement in the mechanism of action of
1765 hallucinogenic agents. *Life Sci.* **35**, 2505–2511 (1984).
1766 77. López-Giménez, J. F. & González-Maeso, J. Hallucinogens and serotonin 5-HT2A receptor-mediated signaling
1767 pathways. *Curr. Top. Behav. Neurosci.* **36**, 45–73 (2018).
1768 78. Cookson, J. & Jonsson, F. A new cholinergic mechanism for antipsychotics: emraclidine and M4 muscarinic
1769 receptors. *Lancet* **400**, 2159–2161 (2022).
1770 79. Kaul, I. *et al.* Efficacy and safety of the muscarinic receptor agonist KarXT (xanomeline–trospium) in
1771 schizophrenia (EMERGENT-2) in the USA: results from a randomised, double-blind, placebo-controlled,
1772 flexible-dose phase 3 trial. *Lancet* **403**, 160–170 (2024).
1773 80. Shamah, S. M. *et al.* EphA Receptors Regulate Growth Cone Dynamics through the Novel Guanine Nucleotide
1774 Exchange Factor Ephexin. *Cell* **105**, 233–244 (2001).
1775 81. Frisén, J., Holmberg, J. & Barbacid, M. Ephrins and their Eph receptors: multitalented directors of embryonic
1776 development. *EMBO J.* **18**, 5159-5165–5165 (1999).
1777 82. Williams, M. E. *et al.* Cadherin-9 regulates synapse-specific differentiation in the developing hippocampus.
1778 *Neuron* **71**, 640–655 (2011).
1779 83. Gerfen, C. R. Segregation of D1 and D2 dopamine receptors in the striatal direct and indirect pathways: An
1780 historical perspective. *Front. Synaptic Neurosci.* **14**, 1002960 (2022).
1781 84. Aringhieri, S. *et al.* Molecular targets of atypical antipsychotics: From mechanism of action to clinical
1782 differences. *Pharmacol. Ther.* **192**, 20–41 (2018).
1783 85. Lew, J. Y. *et al.* Increased site-specific phosphorylation of tyrosine hydroxylase accompanies stimulation of

1784 enzymatic activity induced by cessation of dopamine neuronal activity. *Mol. Pharmacol.* **55**, 202–209 (1999).
1785 86. Lindgren, N. *et al.* Regulation of tyrosine hydroxylase activity and phosphorylation at Ser(19) and Ser(40) via
1786 activation of glutamate NMDA receptors in rat striatum. *J. Neurochem.* **74**, 2470–2477 (2000).
1787 87. Nagai, T. *et al.* Phosphoproteomics of the Dopamine Pathway Enables Discovery of Rap1 Activation as a
1788 Reward Signal In Vivo. *Neuron* **89**, 550–565 (2016).
1789 88. Kimmel, H. L., Gong, W., Vechia, S. D., Hunter, R. G. & Kuhar, M. J. Intra-ventral tegmental area injection of rat
1790 cocaine and amphetamine-regulated transcript peptide 55-102 induces locomotor activity and promotes
1791 conditioned place preference. *J. Pharmacol. Exp. Ther.* **294**, 784–792 (2000).
1792 89. Hubert, G. W., Jones, D. C., Moffett, M. C., Rogge, G. & Kuhar, M. J. CART peptides as modulators of
1793 dopamine and psychostimulants and interactions with the mesolimbic dopaminergic system. *Biochem.*
1794 *Pharmacol.* **75**, 57–62 (2008).
1795 90. Chen, Y., Saulnier, J. L., Yellen, G. & Sabatini, B. L. A PKA activity sensor for quantitative analysis of
1796 endogenous GPCR signaling via 2-photon FRET-FLIM imaging. *Front. Pharmacol.* **5**, 56 (2014).
1797 91. Lee, S. J., Chen, Y., Lodder, B. & Sabatini, B. L. Monitoring Behaviorally Induced Biochemical Changes Using
1798 Fluorescence Lifetime Photometry. *Front. Neurosci.* **13**, 766 (2019).
1799 92. Jentsch, J. D., Roth, R. H. & Taylor, J. R. Role for dopamine in the behavioral functions of the prefrontal
1800 corticostriatal system: implications for mental disorders and psychotropic drug action. *Prog. Brain Res.* **126**,
1801 433–453 (2000).
1802 93. Grace, A. A. Dysregulation of the dopamine system in the pathophysiology of schizophrenia and depression.
1803 *Nat. Rev. Neurosci.* **17**, 524–532 (2016).
1804 94. Thomas, E. A. Molecular profiling of antipsychotic drug function: convergent mechanisms in the pathology and
1805 treatment of psychiatric disorders. *Mol. Neurobiol.* **34**, 109–128 (2006).
1806 95. Lee, S. J. *et al.* Cell-type-specific asynchronous modulation of PKA by dopamine in learning. *Nature* **590**, 451–
1807 456 (2021).
1808 96. Graybiel, A. M. & Grafton, S. T. The striatum: where skills and habits meet. *Cold Spring Harb. Perspect. Biol.* **7**,
1809 a021691 (2015).
1810 97. Breier, A. *et al.* Schizophrenia is associated with elevated amphetamine-induced synaptic dopamine
1811 concentrations: evidence from a novel positron emission tomography method. *Proc. Natl. Acad. Sci. U. S. A.* **94**,
1812 2569–2574 (1997).
1813 98. Wang, S. *et al.* Loss-of-function variants in the schizophrenia risk gene SETD1A alter neuronal network activity
1814 in human neurons through the cAMP/PKA pathway. *Cell Rep.* **39**, 110790 (2022).

1815 99. Dejanovic, B. *et al.* Changes in the Synaptic Proteome in Tauopathy and Rescue of Tau-Induced Synapse Loss
1816 by C1q Antibodies. *Neuron* **100**, 1322-1336.e7 (2018).
1817 100. Dejanovic, B. *et al.* Complement C1q-dependent excitatory and inhibitory synapse elimination by astrocytes and
1818 microglia in Alzheimer's disease mouse models. *Nat Aging* **2**, 837–850 (2022).
1819 101. UniProt Consortium. UniProt: the universal protein knowledgebase in 2021. *Nucleic Acids Res.* **49**, D480–D489
1820 (2021).
1821 102. Zhou, X. L. *et al.* ROR2 modulates neuropathic pain via phosphorylation of NMDA receptor subunit GluN2B in
1822 rats. *Br. J. Anaesth.* **123**, e239–e248 (2019).
1823 103. Morshed, N. *et al.* Phosphoproteomics identifies microglial Siglec-F inflammatory response during
1824 neurodegeneration. *Mol. Syst. Biol.* **16**, e9819 (2020).
1825 104. O'Shea, J. P. *et al.* pLogo: a probabilistic approach to visualizing sequence motifs. *Nat. Methods* **10**, 1211–1212
1826 (2013).
1827 105. Biancalani, T. *et al.* Deep learning and alignment of spatially resolved single-cell transcriptomes with Tangram.
1828 *Nat. Methods* **18**, 1352–1362 (2021).
1829 106. Di Tommaso, P. *et al.* Nextflow enables reproducible computational workflows. *Nat. Biotechnol.* **35**, 316–319
1830 (2017).
1831 107. Patro, R., Duggal, G., Love, M. I., Irizarry, R. A. & Kingsford, C. Salmon provides fast and bias-aware
1832 quantification of transcript expression. *Nat. Methods* **14**, 417–419 (2017).
1833 108. Love, M. I., Huber, W. & Anders, S. Moderated estimation of fold change and dispersion for RNA-seq data with
1834 DESeq2. *Genome Biol.* **15**, 550 (2014).
1835 109. Soneson, C., Love, M. I. & Robinson, M. D. Differential analyses for RNA-seq: transcript-level estimates
1836 improve gene-level inferences. *F1000Res.* **4**, 1521 (2015).
1837 110. Zheng, G. X. Y. *et al.* Massively parallel digital transcriptional profiling of single cells. *Nat. Commun.* **8**, 1–12
1838 (2017).
1839 111. Stuart, T. *et al.* Comprehensive Integration of Single-Cell Data. *Cell* **177**, 1888-1902.e21 (2019).
1840 112. Wolock, S. L., Lopez, R. & Klein, A. M. Scrublet: Computational Identification of Cell Doublets in Single-Cell
1841 Transcriptomic Data. *Cell Syst* **8**, 281-291.e9 (2019).
1842 113. Ding, J. *et al.* Systematic comparison of single-cell and single-nucleus RNA-sequencing methods. *Nat.*
1843 *Biotechnol.* **38**, 737–746 (2020).
1844 114. Zeisel, A. *et al.* Molecular Architecture of the Mouse Nervous System. *Cell* **174**, 999-1014.e22 (2018).
1845 115. Saunders, A. *et al.* Molecular Diversity and Specializations among the Cells of the Adult Mouse Brain. *Cell* **174**,

1846 1015-1030.e16 (2018).
1847 116. Leek, J. T., Johnson, W. E., Parker, H. S., Jaffe, A. E. & Storey, J. D. The sva package for removing batch
1848 effects and other unwanted variation in high-throughput experiments. *Bioinformatics* **28**, 882–883 (2012).
1849 117. Robinson, M. D., McCarthy, D. J. & Smyth, G. K. edgeR: a Bioconductor package for differential expression
1850 analysis of digital gene expression data. *Bioinformatics* **26**, 139–140 (2010).
1851 118. Phipson, B. *et al.* propeller: testing for differences in cell type proportions in single cell data. *Bioinformatics* **38**,
1852 4720–4726 (2022).
1853 119. Savell, K. E. *et al.* A dopamine-induced gene expression signature regulates neuronal function and cocaine
1854 response. *Sci Adv* **6**, eaba4221 (2020).